



#### Available online at www.sciencedirect.com

# **ScienceDirect**

Comput. Methods Appl. Mech. Engrg. 358 (2020) 112615

Computer methods in applied mechanics and engineering

www.elsevier.com/locate/cma

# Experimental validation of a variational data assimilation procedure for estimating space-dependent cardiac conductivities

Alessandro Barone<sup>a</sup>, Alessio Gizzi<sup>b</sup>, Flavio Fenton<sup>c</sup>, Simonetta Filippi<sup>b</sup>, Alessandro Veneziani<sup>a,d,\*</sup>

<sup>a</sup> Department of Mathematics, Emory University, Atlanta, GA, USA

<sup>b</sup> Nonlinear Physics and Mathematical Modeling Laboratory, University Campus Bio-Medico of Rome, Rome, Italy

<sup>c</sup> School of Physics, Georgia Institute of Technology, Atlanta, GA, USA

<sup>d</sup> Department of Computer Science, Emory University, Atlanta, GA, USA

Available online 16 September 2019

#### **Highlights**

- Target: identification of cardiac conductivities from potential measures.
- Method: variational approach based on constrained minimization and Lagrange multipliers.
- Design 1: conductivities for the Monodomain system are assumed space-dependent.
- Design 2: different ionic models are considered (Fenton-Karma, Mitchell-Schaeffer).
- Results: extensive validation on ex-vivo models successfully confirm the reliability of the approach.

# Abstract

Customization of mathematical and numerical models to patient-specific settings is a critical step of the translation process bringing scientific computing to the clinical activity. In cardiovascular diseases, this process is at an advanced stage. It requires image processing for patient morphology retrieval and data assimilation for the calibration of the parameters of the model. Different methods of data assimilation are available for calibrating parameters from measures and an accurate assessment of their reliability in realistic scenarios is not trivial. In this paper, we consider the estimation of cardiac space-dependent conductivities for the Monodomain modeling of the propagation of the excitation potential in the heart with a variational deterministic approach. We perform an extensive validation of our method based on experimental data obtained by fluorescence optical mapping recordings on animal models. The results demonstrate that our procedure provides reliable results when coupled with phenomenological ionic models like the Fenton–Karma and the Mitchell–Schaeffer ones. These promising results give confidence that our approach could be used in clinical scenarios for applying computational techniques to support the decision-making process of medical doctors, like, e.g., the optimal placement of pacemakers.

© 2019 Elsevier B.V. All rights reserved.

Keywords: Cardiac electrophysiology; Reaction-diffusion; Parameter identification; Data assimilation; Optical mapping; Cardiac conductivities

<sup>\*</sup> Corresponding author at: Department of Mathematics, Emory University, Atlanta, GA, USA. *E-mail addresses:* abaron2@emory.edu (A. Barone), a.gizzi@unicampus.it (A. Gizzi), flavio.fenton@physics.gatech.edu (F. Fenton), s.filippi@unicampus.it (S. Filippi), avenez2@emory.edu (A. Veneziani).

#### 1. Introduction

Mathematical and numerical modeling in electrophysiology is a mature field of applied and computational mathematics, supported by an abundant and comprehensive literature [1-4] (to mention a few). One of the most significant challenges to face is the translation process of quantitative modeling to the clinical practice. In fact, many mathematical tools have been developed in the last years to address clinical problems, like the rigorous interpretation of ECG [5] or the therapy optimization for propagation disorders [6-8]. However, the transitional process requires (1) an educated selection of the numerical models as the trade-off between accuracy and efficiency, and (2) an accurate customization of the mathematical models and, more specifically, a fine tuning of the many parameters featured by the relevant equations on patient-specific data. As a matter of fact, the models for the electrical (transmembrane voltage) propagation in the cardiac tissue feature, in general, many parameters, and their accurate quantification is not easy, particularly when considering clinical or, more in general, in vivo conditions. This last step is relevant for the work presented here and it attains the so-called data assimilation step [9]. We focus on a variational procedure for estimating the cardiac conductivities by transmembrane voltage measurements, in what has been called the Monodomain Inverse Conductivity Problem (MICP). Conductivities were experimentally measured in vitro in 1971 by Geselowitz [10]. Successively, measurements of the intracellular and extracellular conductivities were carried out in different ways by several groups [11–13], leading to disparate ranges of possible values with no common agreement on the most accurate ones. As pointed out in [14,15], an accurate estimate of these coefficients is critical, as they have a major impact on the solution of the mathematical models describing the potential propagation in the tissue. For this reason, computational techniques of estimation have been introduced [16-18]. A variational data assimilation procedure was proposed in [19] and successively analyzed in [20], with the formalization of the MICP that we are considering here.

As a matter of fact, there are two main options available in the literature for describing the propagation of transmembrane voltage, namely the *Monodomain* and the *Bidomain models*. They stem from a homogenization of the tissue microstructural features and, in particular, of the intra- and extra-cellular spaces. The formulation of the Bidomain model is the result of the application of basic principles (conservation of charge) and constitutive models. The Monodomain system can be then obtained as a reduction of the Bidomain one, upon application of some simplifying assumption on the conductivity tensor. The Bidomain model includes a comprehensive description, including both the intra and the extracellular (or, equivalently, the transmembrane) potential. It is well-known that this precise description (and its virtual electrode effect [21]) is crucial when simulating defibrillation protocols during fibrillation scenarios [22,23]. Nevertheless, the Monodomain system can still be the model of choice in specific applications [4]. It has been intensively used in clinical applications [24] since it requires significantly less computational efforts than the Bidomain model. Moreover, it may serve as a powerful auxiliary tool to efficiently solve the Bidomain system [25–27].

In the present work we do restrict our attention to the Monodomain system. In fact, on the one hand we aim at providing a tool for clinical applications, on the other one, we will consider planar waves of cardiac excitation during regular pacing [28] for which the Bidomain and Monodomain formulations ensure the same level of accuracy. However, it is worth stressing that the MICP can be regarded as an intermediate step to perform a more complete conductivity estimation in the Bidomain model, particularly when aiming at estimating a space-dependent conductivity. An accurate estimation of the conductivity tensor that characterizes the Monodomain has been proved to lead to an accurate reconstruction of the potential propagation generated by the Bidomain equations [15,29].

The MICP has been considered previously in a number of works [15,19,20,29], covering both theoretical aspects, its effective numerical approximation and sensitivity of the results on the measures. So far, we have considered only synthetic tests, where the measures were generated by numerical simulations added by a synthetic noise. The specific purpose of the present work is to perform an extensive validation on *experimental data*. This is, in fact, a fundamental step in assessing the actual reliability of the variational procedure in real problems, with actual experimental settings that generally may differ from synthetic benchmarks.

Specifically, we present the problem in Sections 2 (forward problem) and 3 (inverse problem). A preliminary testing on synthetic data for the calibration of the parameters of the inverse problem solving is presented in Section 4. The experimental setting is described in Section 5 with the extensive comparison among numerical results from three different electrophysiological models and data and the associated discussion. Conclusions and perspectives are drawn in Section 6.

List of abbreviations

For the sake of readability, we add a list of the abbreviations used in the manuscript.

AP (Action Potential), APD (Action Potential Duration), BZ (Border Zone), CL (Cycle Length), CV (Conduction Velocity), DO (Discretize-then-Optimize), DOFs (Degrees of Freedom), FK (Fenton–Karma), MICP (Monodomain Inverse Conductivity Problem), MM (Minimal Model), MS (Mitchell–Schaeffer), OD (Optimize-then-Discretize), RC (Restitution Curve).

#### 2. Models

We provide a short summary of the equations of Monodomain models, referring to the literature for a more comprehensive introduction to the subject [2]. This system of partial differential equations (as well as the Bidomain one) requires constitutive laws describing the ionic dynamics in the cardiac tissue, generally denoted by *ionic models*. Their complexity depends on the number of ionic currents included in the description [4]. We consider here three possible models previously proposed, characterized by an increasing level of complexity.

The monodomain model. The backbone of the Monodomain model consists of a reaction—diffusion system of equations. The balance of ionic fluxes through the cell membrane in both the longitudinal and transversal directions is accounted for by a diffusive Partial Differential Equation (PDE) in which the reaction term specifies the number of currents considered in the model. Besides, the ionic model consists of a list of coupled Ordinary Differential Equations (ODEs) describing the reaction kinetics of selected ionic currents (see e.g. [30] for details).

On these assumptions, the Monodomain model reads

$$\begin{cases} \partial_t u = \nabla \cdot (\boldsymbol{\sigma}(\mathbf{x}) \nabla u) - I_{ion}(u, \mathbf{w}) + I_{app} \\ \mathbf{d}_t \mathbf{w} = \mathbf{g}(u, \mathbf{w}) \end{cases} \quad \text{in } Q$$
 (1)

with initial and boundary conditions

$$\begin{cases} u(\mathbf{x}, 0) = u_0(\mathbf{x}), & \mathbf{w}(\mathbf{x}, 0) = \mathbf{w}_0(\mathbf{x}) & \text{in } \Omega \\ \sigma(\mathbf{x}) \nabla u \cdot \mathbf{n} = 0 & \text{on } \partial Q. \end{cases}$$
 (2)

Here,  $Q = \Omega \times [0, T]$ ;  $\partial Q = \partial \Omega \times [0, T]$ ;  $\Omega \subset \mathbb{R}^d$  (d = 2 or 3) is a bounded domain; [0, T] a fixed time interval;  $\mathbf{x}$  the spatial coordinates; u the (dimensionless) transmembrane potential;  $\mathbf{w}$  the vector of the so called gating variables characterizing the ionic model;  $\sigma(\mathbf{x})$  the conductivity tensor, in general function of the local coordinates;  $I_{ion}(u, \mathbf{w})$  the total ionic current flowing through the membrane;  $\mathbf{g}(u, \mathbf{w})$  the kinetic dynamics of the ionic quantities;  $I_{app}$  the external stimulation current (e.g. electrical pacing or synaptic input);  $\mathbf{n}$  the outward unit normal vector on the boundary  $\partial \Omega$ . As usual, the symbols  $\partial_t$ ,  $d_t$ ,  $\nabla$  and  $\nabla$  represent the partial and total derivatives with respect to time, the spatial gradient and divergence operators, respectively. Condition  $(2)_2$  is of Neumann-type, usually adopted in the present context [1]. In physical terms, it tries to mimic an insulated tissue. From a mathematical point of view, it is well known that Neumann-type conditions, though an approximation of the complex phenomenology, minimize the sensitivity of arbitrary data on the simulation results [31].

A relevant issue for the purpose of the present work is the representation of the conductivity tensor in the context of a complex orthotropic three-dimensional tissue. We refer to the cardiac fibers principal directions [1,32]. In detail, let  $(a_l, a_t, a_n)$  be the orthonormal fields related to the structure of the myocardium with  $a_l$  the longitudinal fiber direction,  $a_t$  and  $a_n$  the orthogonal directions to the fiber in the sheet and orthogonal to the sheet, respectively. Accordingly, we can decompose the conductivity tensor as:

$$\sigma(\mathbf{x}) = \sigma_l(\mathbf{x})\mathbf{a_l}\mathbf{a_l}^T + \sigma_t(\mathbf{x})\mathbf{a_t}\mathbf{a_t}^T + \sigma_n(\mathbf{x})\mathbf{a_n}\mathbf{a_n}^T,$$

where  $\sigma_l$ ,  $\sigma_t$ ,  $\sigma_n$  denote the longitudinal-, tangential- and normal-to-the-fiber conductivities, respectively.

In the following, based on two-dimensional optical data, we assume that the tissue can be conveniently described as a transverse isotropic material (i.e.  $\sigma_t(\mathbf{x}) = \sigma_n(\mathbf{x})$ ) and the tensor simplifies to

$$\sigma(\mathbf{x}) = \sigma_t(\mathbf{x})\mathbf{I} + (\sigma_l(\mathbf{x}) - \sigma_t(\mathbf{x}))\mathbf{a}_l\mathbf{a}_l^T, \tag{3}$$

where **I** is the  $d \times d$  identity tensor.

*Ionic models*. As we aim at introducing a reliable and effective data assimilation procedure for cardiac electrophysiology, we deliberately chose a simplified phenomenological approach to reproduce the electrical behavior of ventricular cardiac cells. Specifically, we consider three possible ionic models, the Mitchell–Schaeffer (MS) model [33], the Fenton–Karma (FK) model [34], and the Minimal model (MM) [35]. The specific description of the time evolution of  $\mathbf{w}$  in Eq. (1) and the associated nonlinear reaction function  $I_{ion}(u, \mathbf{w})$  are provided according to the level of complexity inherent the specific model. In fact, MS, FK and MM models are characterized by two, three and four variables respectively, with associated 2, 3, and 3 ionic currents and 5, 12, and 28 constitutive parameters.

The study and parametric characterization of ionic models rely on both local- and global-in-space/time features. The space and time course of the transmembrane voltage following an electrical stimulation, i.e. an elicited action potential (AP) excitation wave, has been historically linked to specific measurable subfeatures of the AP wave, i.e. the Action Potential Duration (APD) and the Conduction Velocity (CV) (see [36] for details). In what follows, we will specifically use the Restitution Curve (RC), describing the dependence of APD on the pacing cycle length to adopt a convenient set of modeling parameters qualitatively reproducing the observed behavior. State-of-the-art fitting genetic algorithms [37] may provide an accurate estimation of those parameters, but they are not the focus of the present work. We empirically identify a good-enough approximation of AP shape and restitution curves. Such a choice allows us to prove the reliability of our data assimilation methodology also in presence of poor fitting power or high experimental error. The model parameters are reported in Table 1.

The Mitchell–Schaeffer model. The MS model is a FitzHugh–Nagumo-like phenomenological model [30] (it can also be read as simplification of the FK model) that qualitatively reproduces cardiac action potential dynamics and restitution features. Thanks to its simplicity, the model is numerically efficient. In addition, it is possible to carry out a comprehensive sensitivity analysis on its-parameters; last but not least, it is possible to derive from the reaction–diffusion model an explicit formula for the restitution curve [33].

The MS reaction kinetics for  $(\mathbf{w} = [v])$  reads:

$$d_t v = (1 - v)/\tau_{open} - \left[v/\tau_{close} + (1 - v)/\tau_{open}\right]H(u - u_{gate}) \tag{4}$$

where  $I_{ion}(u, \mathbf{w})$  is given by the sum of two currents, inward and outward, respectively:

$$J_{in} = vu^2(1-u)/\tau_{in}, \qquad J_{out} = u/\tau_{out},$$
 (5)

with  $u \in [0, 1]$ ;  $H(\cdot)$  is the standard Heaviside step function.

The Fenton–Karma model. The FK model is a generalization of the two-variable Karma model [38] able to properly approximate time course, restitution properties and spiral wave dynamics of the cardiac AP excitation wave [34,39]. Although the model does not reproduce realistic AP shapes (in particular the spike-and-dome behavior of myocardial cells), it is complex enough to exhibit many of the characteristics of cardiac cells, but also simple enough that much of its behavior can be understood analytically.

Model equations are  $(\mathbf{w} = [v, w])$ 

$$d_t v = H(u_c - u)(1 - v)/\tau_v^-(u) - H(u - u_c)v/\tau_v^+ d_t w = H(u_c - u)(1 - w)/\tau_w^- - H(u - u_c)w/\tau_w^+$$
(6)

where  $I_{ion}(u, \mathbf{w})$  is given by the sum of three currents, fast inward  $J_{fi}$ , slow outward  $J_{so}$ , and slow inward  $J_{si}$ , respectively:

$$J_{fi} = -vH(u - u_c)(1 - u)(u - u_c)/\tau_d$$

$$J_{so} = uH(u_c - u)/\tau_o + H(u - u_c)/\tau_r$$

$$J_{si} = -w[1 + \tanh(k(u - u_c^{si}))]/2\tau_{si},$$
(7)

and the voltage-dependent time constant is

$$\tau_{v}^{-}(u) = H(u - u_{v})\tau_{v1}^{-} + H(u_{v} - u)\tau_{v2}^{-}, \tag{8}$$

with  $u \in [0, 1]$ .

Table 1

Ionic models parameters tuned to qualitatively reproduce the time course of the action potential signal and the restitution curves. Time is in unit of ms.

MS p	arameters	S											
$ au_{in}$			$ au_{out}$			$ au_{close}$			$ au_{oper}$	ı			$u_{gate}$
0.3	10		69			220			0.13				
FK pa	arameters	;											
$u_c$	$ au_d$		$\tau_o$	$\tau_r$	k	$u_c^{si}$	$ au_{si}$	$ au_v^+$	$ au_w^-$	$ au_w^+$		$ au_{v1}^-$	$ au_{v2}^-$
0.13	0.	1724	12.5	130	10	0.85	127	1.62	80	10	20	38.2	38.2
MM j	paramete	rs											
$u_o$	$u_u$	$\theta_v$	$\theta_w$	$\theta_v^-$	$\theta_o$	$ au_{v1}^-$	$ au_{w2}^-$	$k_w^-$	$u_w^-$	$ au_w^+$	$ au_{fi}$	$ au_{o1}$	$\tau_{o2}$
0	1.58	0.3	0.015	0.015	0.006	60	20	65	0.03	280	0.11	6	6
$k_{so}$	$u_{so}$	$\tau_{s1}$	$\tau_{s2}$	$k_s$	$u_s$	$ au_{si}$	$ au_{v2}^-$	$ au_v^+$	$ au_{w1}^-$	$\tau_{so1}$	$\tau_{so2}$	$ au_{w\infty}$	$w_{\infty}^*$
2	0.65	2.7342	3	2.0994	0.9087	2.8723	1150	1.4506	70	43	0.2	0.07	0.94

The minimal model. The MM model is based on the FK one with the addition of a fourth variable to adjust the inward current to reproduce the spike-and-dome morphology for myocardial cells. It provides a description of the human and animal ventricular cells reproducing in detail experimentally measured characteristics of action potentials. These characteristics are both at cell and tissue-level including: action potential amplitude and morphology, upstroke conduction velocity (CV) of the excitation wave, APD and CV restitution curves, spatio-temporal alternans and spiral waves as dynamics fundamental features of cardiac arrhythmias [35]. Moreover, it can be fitted to reproduce the dynamics of other – more complex – physiological models, yet it is computationally more efficient. For  $\mathbf{w} = [v, w, s]$ , it reads

$$d_{t}v = [1 - H(u - \theta_{v})](v_{\infty} - v)/\tau_{v}^{-} - H(u - \theta_{v})v/\tau_{v}^{+}$$

$$d_{t}w = [1 - H(u - \theta_{w})](w_{\infty} - w)/\tau_{w}^{-} - H(u - \theta_{w})w/\tau_{w}^{+}$$

$$d_{t}s = \{[1 + \tanh(k_{s}(u - u_{s}))]/2 - s\}/\tau_{s}$$
(9)

where the three currents are given by

$$J_{fi} = -vH(u - \theta_v)(u - \theta_v)(u_u - u)/\tau_{fi}$$

$$J_{si} = -H(u - \theta_w)ws/\tau_{si}$$

$$J_{so} = (u - u_o)[1 - H(u - \theta_w)]/\tau_o + H(u - \theta_w)/\tau_{so}$$
(10)

and the voltage-dependent time constants are

$$\tau_{v}^{-} = \left[1 - H(u - \theta_{v}^{-})\right]\tau_{v1}^{-} + H(u - \theta_{v}^{-})\tau_{v2}^{-} 
\tau_{w}^{-} = \tau_{w1}^{-} + (\tau_{w2}^{-} - \tau_{w1}^{-})\left[1 + \tanh(k_{w}^{-}(u - u_{w}^{-}))\right]/2 
\tau_{so}^{-} = \tau_{so1}^{-} + (\tau_{so2}^{-} - \tau_{so1}^{-})\left[1 + \tanh(k_{so}(u - u_{so}))\right]/2 
\tau_{s} = \left[1 - H(u - \theta_{w})\right]\tau_{s1} + H(u - \theta_{w})\tau_{s2} 
\tau_{o} = \left[1 - H(u - \theta_{o})\right]\tau_{o1} + H(u - \theta_{o})\tau_{o2} 
v_{\infty} = 1 - H(u - \theta_{v}^{-}) 
w_{\infty} = \left[1 - H(u - \theta_{o})\right](1 - u/\tau_{w\infty}) + H(u - \theta_{o})w_{\infty}^{*}.$$
with  $u \in [0, 1.5]$ .

#### 3. The monodomain inverse conductivity problem (MICP)

Let the admissible functional space for the conductivity tensor be  $C_{ad}$ 

$$C_{ad} = \{ \boldsymbol{\sigma} \in \mathbf{H}^1(\Omega) : \boldsymbol{\sigma}(\mathbf{x}) \in [m, M]^d, \forall \mathbf{x} \in \Omega \},\$$

where  $\mathbf{H}^1(\Omega) \equiv (H^1(\Omega))^d$  and m, M are positive constants. Notice that for the solution of the forward Monodomain problem, it would suffice assuming the conductivities as bounded functions  $(L^{\infty}(\Omega))$  of the space variables (e.g., piecewise constant). The same admissible space works for the inverse problem when using a regularization based on the values of the conductivities and not on their (space) derivatives, as done in [20]. However, here we need additional regularization terms, so we restrict our admissible space to  $\mathcal{C}_{ad}$ .

The *Monodomain inverse conductivity problem* (MICP) aims at finding the tensor  $\sigma(\mathbf{x}) \in \mathcal{C}_{ad}$  minimizing the misfit functional  $\mathcal{J}$  [19]:

$$\mathcal{J}(\boldsymbol{\sigma}(\mathbf{x})) = \frac{1}{2} \int_0^T \int_{\Omega_{obs}} \left( u(\boldsymbol{\sigma}(\mathbf{x})) - u_{meas} \right)^2 d\mathbf{x} dt + \mathcal{R}(\boldsymbol{\sigma})$$
(12)

subject to (1) and (2). Here,  $u_{meas}$  denotes the experimental data measured on the observation domain  $\Omega_{obs} \subset \Omega$ .  $\mathcal{R}(\sigma)$  is a Tikhonov-like regularization term that in our formulation reads

$$\mathcal{R}(\boldsymbol{\sigma}) = \frac{\alpha_1}{2} \left( \|\nabla \sigma_l(\mathbf{x})\|^2 + \|\nabla \sigma_t(\mathbf{x})\|^2 \right) + \frac{\alpha_2}{2} \left( \|\sigma_l(\mathbf{x}) - \sigma_{l,mean}(\mathbf{x})\|^2 + \|\sigma_t(\mathbf{x}) - \sigma_{t,mean}(\mathbf{x})\|^2 \right),$$
(13)

where  $\sigma_{l,mean}$  and  $\sigma_{t,mean}$  denote an average of available conductivity values from literature,  $\alpha_1, \alpha_2$  are regularization coefficients weighting the impact of the regularization on the minimization procedure, and  $\|\cdot\|$  the  $L^2$ -norm.

The method of Lagrange multipliers is a possible approach to solve the constrained optimization problem [20]. Following this approach, the MICP Lagrangian functional reads

$$\mathcal{L}(u, \mathbf{w}, \boldsymbol{\sigma}, q, \mathbf{r}) = \mathcal{J}(\boldsymbol{\sigma}) - \int_{0}^{T} \int_{\Omega} q \left( \partial_{t} u - \nabla \cdot (\boldsymbol{\sigma} \nabla u) + I_{ion}(u, \mathbf{w}) - I_{app} \right) d\mathbf{x} dt - \int_{0}^{T} \int_{\Omega} \mathbf{r} \cdot \left( d_{t} \mathbf{w} - \mathbf{g}(u, \mathbf{w}) \right) d\mathbf{x} dt,$$

$$(14)$$

where  $q(\mathbf{x},t)$  and  $\mathbf{r}(\mathbf{x},t)$  are the Lagrange multipliers;  $(u,q) \in (L^2(0,T;H^1(\Omega)))^2$ ,  $(\mathbf{w},\mathbf{r}) \in (L^2(0,T;L^2(\Omega)))^{2g}$ , where g is the number of gating variables of the ionic model;  $I_{app} \in L^2(0,T;(H^1(\Omega))^*)$ , where  $(H^1(\Omega))^*$  denotes the dual space of  $H^1(\Omega)$ . According to this approach [40], the solution is obtained by finding the critical points of the functional with respect to the state variables u and  $\mathbf{w}$ , the Lagrange multipliers and the control variable  $\sigma$ . This leads to the so called Karush–Kuhn–Tucker (KKT) system. In particular, the Gateaux differentials with respect to the Lagrange multipliers give the constraint equations, i.e. the monodomain problem (1) (with the appropriate ionic model). Setting the partial derivatives  $\partial \mathcal{L}/\partial u$  and  $\partial \mathcal{L}/\partial \mathbf{w}$  equal to zero, we construct the *adjoint equations* 

II). Setting the partial derivatives 
$$\partial \mathcal{L}/\partial u$$
 and  $\partial \mathcal{L}/\partial \mathbf{w}$  equal to zero, we construct the *adjoint equations*

$$\begin{cases}
-\partial_t q = \nabla \cdot (\boldsymbol{\sigma} \nabla q) - \partial_u \mathbf{g} \cdot \mathbf{r} - \partial_u I_{ion}(u, \mathbf{w}) q + (u - u_{meas}) \chi_{\Omega_{obs}} & \text{in } Q \\
\partial_t \mathbf{r} = \partial_{\mathbf{w}} \mathbf{g} \cdot \mathbf{r} + \partial_{\mathbf{w}} I_{ion}(u, \mathbf{w}) q & \text{in } Q \\
\boldsymbol{\sigma} \nabla q \cdot \mathbf{n} = 0 & \text{on } \partial Q \\
q(\mathbf{x}, T) = 0, \quad \mathbf{r}(\mathbf{x}, T) = \mathbf{0} & \text{in } \Omega,
\end{cases}$$
(15)

where  $\chi_{\Omega_{obs}}$  is the indicator function of the observation domain  $\Omega_{obs}$ . Notice that this problem is backward in time. Based on the adjoint equations, we get the Gateaux derivatives of J as follows

$$\frac{\mathcal{D}\mathcal{J}}{\mathcal{D}\sigma_k} = \frac{\partial \mathcal{L}}{\partial \sigma_k} = -\int_0^T \mathbf{a_k} \mathbf{a_k}^T \nabla u \cdot \nabla q \, dt + \frac{\partial \mathcal{R}}{\partial \sigma_k}, \quad \text{with} \quad k = l, t.$$
 (16)

A partial well-posedness analysis of MICP can be found in [20].

In practice, the KKT system is solved following an iterative approach. For a given initial guess of the control variable  $\sigma^{(0)}$  and setting k = 0, we solve:

- (i) the Monodomain system (1) with the current guess for the conductivity so to compute  $u^k$  and  $\mathbf{w}^k$ ;
- (ii) the adjoint problem (15) with the current guess for the conductivity and state variables so to obtain  $q^k$  and  $\mathbf{r}^k$ ;
- (iii) the optimality conditions (16) to obtain the new approximation  $\sigma^{(k+1)}$  and set k=k+1.

These iterations end when a convergence test is fulfilled.

# 3.1. Numerical approximation of the MICP

Following a quite consolidated strategy – e.g. [25] – we decouple the PDE system and the ODEs ionic model. The time advancing scheme for the ODEs and the PDE is a backward differentiation formula (BDF) method of order 2, whereas we use FEM for the space discretization. The conductivity fields  $\sigma_l(\mathbf{x})$  and  $\sigma_t(\mathbf{x})$  are approximated with piecewise linear (P1) finite elements on a coarse mesh, i.e.,  $\sigma_{k,h}(\mathbf{x}) = \sum_{i=1}^{N} \sigma_k^i \phi_i(\mathbf{x})$ , where k = l, t; N is the number of DOFs of the coarse mesh; and  $\{\phi_j\}_{j=1}^{N}$  are the generic (Lagrange) basis functions of the finite-dimensional subspace of  $H^1$  of piecewise linear functions with dimension N. Moreover

$$\frac{\mathcal{D}\mathcal{J}}{\mathcal{D}\sigma_{k,h}(\mathbf{x})} = \sum_{l=1}^{N} \frac{\mathcal{D}\mathcal{J}}{\mathcal{D}\sigma_{k}^{l}} \phi_{l}(\mathbf{x})$$

and  $\mathcal{D}\mathcal{J}/\mathcal{D}\sigma_k^l$ ,  $\forall l=1,\ldots,N$ , can be determined as

$$\left\langle \sum_{l=1}^{N} \frac{\mathcal{D}\mathcal{J}}{\mathcal{D}\sigma_{k}^{l}} \phi_{l}(\mathbf{x}), \phi_{j}(\mathbf{x}) \right\rangle = -\int_{0}^{T} \int_{\Omega} \mathbf{a}_{k} \mathbf{a}_{k}^{T} \nabla u \cdot \nabla q \phi_{j}(\mathbf{x}) \, d\mathbf{x} dt + \int_{\Omega} \frac{\partial \mathcal{R}}{\partial \sigma_{k}} \phi_{j}(\mathbf{x}) \, d\mathbf{x}.$$

By definition of  $\langle \cdot, \cdot \rangle$ ,

$$\left\langle \sum_{l=1}^{N} \frac{\mathcal{D}\mathcal{J}}{\mathcal{D}\sigma_{k}^{l}} \phi_{l}(\mathbf{x}), \phi_{j}(\mathbf{x}) \right\rangle = \int_{\Omega} \sum_{l=1}^{N} \frac{\mathcal{D}\mathcal{J}}{\mathcal{D}\sigma_{k}^{l}} \phi_{l}(\mathbf{x}) \cdot \phi_{j}(\mathbf{x}) d\mathbf{x},$$

accordingly, we have

$$\frac{\mathcal{D}\mathcal{J}}{\mathcal{D}\sigma_{k,h}(\mathbf{x})} = \mathbf{M}_{coarse} \frac{\mathcal{D}\mathcal{J}}{\mathcal{D}\sigma_k}, \quad \frac{\mathcal{D}\mathcal{J}}{\mathcal{D}\sigma_k} = \left[\frac{\mathcal{D}\mathcal{J}}{\mathcal{D}\sigma_k^l}\right], \ l = 1, \dots, N$$

where  $\mathbf{M}_{coarse}$  is the mass matrix related to the coarse mesh with entries  $[\mathbf{M}_{coarse}]_{jl} = \int_{\Omega} \phi_l(\mathbf{x}) \phi_j(\mathbf{x}) d\mathbf{x}$ . Therefore,  $\mathcal{D} \mathcal{J}/\mathcal{D} \sigma_k$  can be computed as the solution of the linear system

$$\mathbf{M}_{coarse} \frac{\mathcal{D}\mathcal{J}}{\mathcal{D}\sigma_k} = \mathbf{f},$$

where

$$\mathbf{f} = [f_j], \quad f_j = -\int_0^T \int_{\Omega} \mathbf{a_k} \mathbf{a_k}^T \nabla u \cdot \nabla q \phi_j(\mathbf{x}) \, d\mathbf{x} dt + \int_{\Omega} \frac{\partial \mathcal{R}}{\partial \sigma_k} \phi_j(\mathbf{x}) \, d\mathbf{x}$$

for j = 1, ..., N.

The transmembrane potential is approximated on a fine mesh with M DOFs so that the finite element solution reads  $u_h(\mathbf{x}, t) = \sum_{j=1}^{M} u_j(t)\varphi_j(\mathbf{x})$ , where  $\{\varphi_j\}_{j=1}^{M}$  are the generic (Lagrange) basis functions of the finite-dimensional subspace of  $H^1$  of piecewise linear functions with dimension M.

The strategy used to compute  $f_i$  is the following. At time t, we have that

$$-\int_{\Omega} \mathbf{a}_{\mathbf{k}} \mathbf{a}_{\mathbf{k}}^{T} \nabla u \cdot \nabla q \phi_{j}(\mathbf{x}) d\mathbf{x} + \int_{\Omega} \frac{\partial \mathcal{R}}{\partial \sigma_{k}} \phi_{j}(\mathbf{x}) d\mathbf{x} =$$

$$-\int_{\Omega} \mathbf{a}_{\mathbf{k}} \mathbf{a}_{\mathbf{k}}^{T} \sum_{s=1}^{M} u_{s}(t) \nabla \varphi_{s}(\mathbf{x}) \cdot \sum_{v=1}^{M} q_{v}(t) \nabla \varphi_{v}(\mathbf{x}) \phi_{j}(\mathbf{x}) d\mathbf{x} + \int_{\Omega} \frac{\partial \mathcal{R}}{\partial \sigma_{k}} \phi_{j}(\mathbf{x}) d\mathbf{x} =$$

$$-\mathbf{q}^{T} \mathbf{S}_{k}^{j} \mathbf{u} + \int_{\Omega} \frac{\partial \mathcal{R}}{\partial \sigma_{k}} \phi_{j}(\mathbf{x}) d\mathbf{x},$$
(17)

where

$$[\mathbf{S}_k^j]_{sv} = \int_{\mathcal{O}} \mathbf{a}_k \mathbf{a}_k^T \nabla \varphi_v(\mathbf{x}) \cdot \nabla \varphi_s(\mathbf{x}) \phi_j(\mathbf{x}) \, d\mathbf{x}.$$

Finally, we sum up all the contributions for each time step to get  $f_j$ . For more details, we refer to [20]. A specific numerical solution method based on the Proper Orthogonal Decomposition (POD) and the Discrete Empirical Interpolation Method (DEIM) can be found in [29]. In this paper, we focus on the validation, so we refer to a standard numerical approximation.

#### 4. Validation with synthetic data

We present at first some 2D test cases aiming at investigating the accuracy and the efficiency of the variational data assimilation procedure. In a previously published work [15], we performed several synthetic test cases with the Rogers–McCulloch ionic models. In the following tests, we consider the Monodomain model coupled with the MM model in both simple and realistic geometries, in the case of (1) uniform conductivity (both isotropic and anisotropic), (2) space-dependent conductivities. An extensive comparison of the results with the other ionic models is provided in Section 5.

To start with, the computational domain is selected to be a square [0, 6] cm  $\times$  [0, 6] cm. The conductivity fields  $\sigma_l(\mathbf{x})$  and  $\sigma_t(\mathbf{x})$  are defined on a coarse mesh (# DOF = 109) whereas the transmembrane potential is discretized on a finer mesh (# DOF = 94721). For the easiness of the implementation, the meshes are chosen to be nested, i.e., the nodes of the coarse mesh are also nodes of the fine one. Measurements  $u_{meas}$  were recorded every  $dt_{snap} = 2$  ms for a global duration of T = 300 ms. The angle of the cardiac fibers is  $\theta = -43^{\circ}$  with respect to the x-axis, such that no symmetry appears on the squared domain. The observation domain  $\Omega_{obs}$ , where we collect  $u_{meas}$  consists of 8000 equally distributed points on the domain, which is comparable with the number of observation points we can get in experiments.

When solving a numerical optimization problem described by differential equations we generally have to choose between the Optimize-then-Discretize (OD) and the Discretize-then-Optimize (DO) strategies. The two approaches have in general both pros and cons, as excellently pointed out in [41]. Following up our previous work [20], we opted here for the OD approach.

As for any nonlinear iterative problems, the choice of the initial guess is critical both for the final solution (in absence of uniqueness of the solution) as well as the convergence speed. The choice needs to be clearly educated based on the problem at hand and the experience (or the available literature). Yet, this may be not optimal. For this reason, we investigate here two different techniques, hereafter denoted as *Standard* and *Refined*, respectively, for deciding an initial guess  $\sigma_0$ . In the Standard scheme, we perform the optimization procedure globally on the time interval [0, T] as described in previous papers with an initial guess suggested by the experience (trial and error). In the Refined approach, the arbitrary/trial and error initial guess  $\sigma_0$  is improved by adopting the following pre-processing strategy, relying on the time-independence of the conductivities. First, the full time span [0, T] is divided into shorter time intervals of length  $dt_{opt}$ . Then, in each time slot, we perform the optimization using as initial guess the estimation obtained in the previous time interval. Obviously, in the first time interval  $[0, dt_{opt}]$ , the optimization procedure starts from  $\sigma_0$ . Once the last optimization step is performed, the final estimation is used as initial guess of our estimate in the full time interval [0, T]. As we will see later, the overall Refined procedure is convenient as the last estimate will converge more rapidly thanks to the new initial guess, that is supposed to be more informed.

The estimation procedure was implemented in LifeV [42], a parallel finite element library based on the Trilinos software [43], validated against a US Food and Drug Administration benchmark in [44]. Numerical tests for synthetic validation were carried out using 16 cores on a high performance cluster equipped with Intel Xeon L5420 2.5 GHz CPUs. Real validation simulations were performed on Stampede II high performance cluster of the XSEDE consortium using 96 cores on SKX nodes (Intel Xeon Platinum 8160 "Skylake" 2.1 GHz nominal). We chose a standard BFGS for the numerical optimization algorithm of the estimation procedure, together with the following stopping criterion

$$\|\nabla \mathcal{J}(\sigma^k)\| < 10^{-6}$$
 or  $\|\mathcal{J}^k - \mathcal{J}^{k-1}\| < 10^{-6}$  or  $\|\sigma^k - \sigma^{k-1}\| < 10^{-6}$ .

# 4.1. Uniform isotropic conductivity

In the first tests, we aim at assessing the performance of our approach on test cases with a given simple solution assuming uniform conductivity fields in the domain  $\Omega$ . Synthetic data were generated with  $\sigma_{l,exact}(\mathbf{x}) = \sigma_{t,exact}(\mathbf{x}) = 6 \cdot 10^{-3} \text{ cm}^2/\text{ms}$  and Gaussian noise with zero mean and standard deviation equal to  $p \times \max |u|$ , where p is the percentage of noise, and the maximum is taken in both space and time, was added at each time step. A stimulus of intensity  $I_{app} = 0.5 \text{ ms}^{-1}$  is applied at the midpoint of the left edge of the square for a duration of 2 ms. The AP propagation is shown in Fig. 1(a). The initial guess is  $\sigma_{l,0}(\mathbf{x}) = \sigma_{t,0}(\mathbf{x}) = 4 \cdot 10^{-3} \text{ cm}^2/\text{ms}$  and the expected mean conductivity values were taken as  $\sigma_{l,mean}(\mathbf{x}) = \sigma_{t,mean}(\mathbf{x}) = 5 \cdot 10^{-3} \text{ cm}^2/\text{ms}$  (see e.g. [34,39]).

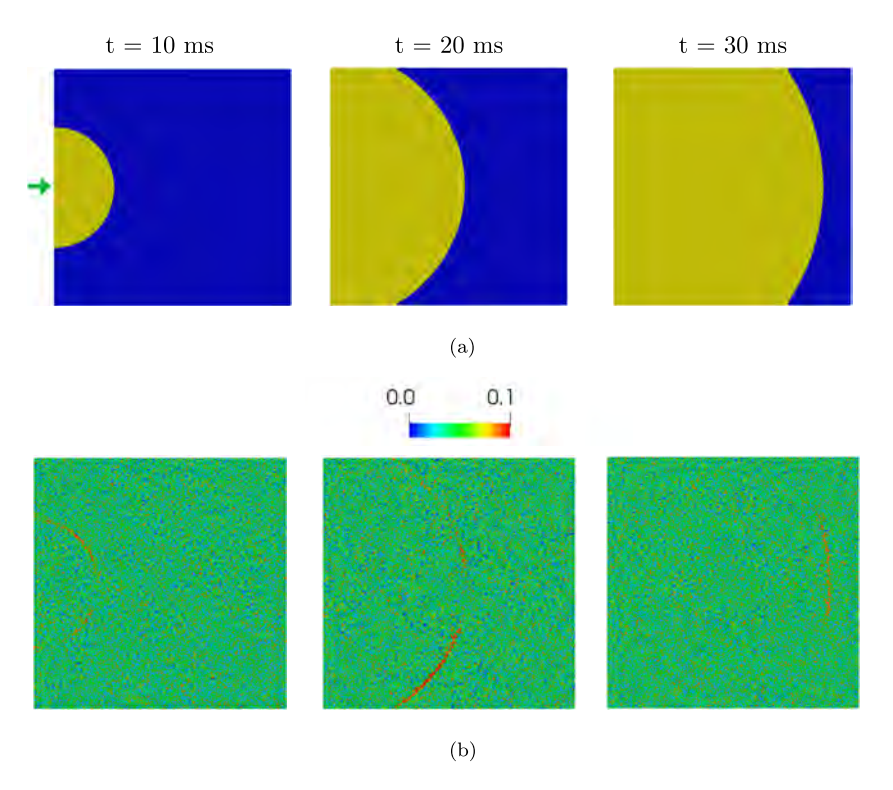


Fig. 1. (a) Isotropic wave propagation at different time steps (contour lines u = 0.75). AP propagates as a symmetric wave from the left to the right edge of the squared domain. Green arrow indicates the site of stimulation. (b) $|u - u_{meas}|$  at different time steps (5% noise).

**Table 2** Comparison between Standard and Refined optimization strategies ( $dt_{opt} = 10$  ms). The Refined scheme provides a more accurate estimation and is computationally cheaper than the standard OD approach. Here, # fwd denotes the number of solves of the state equations, and # bwd represents the number of solves of the adjoint equations.

	$L^2$ error $\sigma_l   \sigma_t$	Exec. time	# fwd bwd
Standard	$4.4 \cdot 10^{-2}   8.0 \cdot 10^{-2} 4.6 \cdot 10^{-3}   2.5 \cdot 10^{-2}$	31.5 h	85 36
Refined		21.0 h	28 19

To investigate the effect on the solutions of the regularization parameters, we performed several estimations with different values of  $\alpha_1$  and  $\alpha_2$  in the range  $[10^{-7}, 1]$ . As well known, this is a critical step in the numerical solution of inverse problems. For large values, the regularization term (13) prevails over the misfit term enforcing the results to be close to the expected (yet, arbitrary) mean conductivity values  $\sigma_{l,mean}(\mathbf{x})$  and  $\sigma_{t,mean}(\mathbf{x})$ . On the other hand, the regularization is critical for the convexity of the functional to minimize and, ultimately, for the convergence of the numerical solver, that may be impaired by exceedingly small values of the parameters. After some experiments, we chose the values  $\alpha_1 = 10^{-4}$  and  $\alpha_2 = 10^{-5}$ . As  $\alpha_2 \ll \alpha_1$  the arbitrary choice of  $\sigma_{l,mean}(\mathbf{x})$  and  $\sigma_{t,mean}(\mathbf{x})$  marginally affects the solution, while gradient regularization results pretty effective for the convergence. Strategies for an automatic tuning of these parameters still need to be pursued.

For the initial guess, Table 2 shows a comparison between the Standard and the Refined algorithms. The Refined scheme outperforms the Standard one, both in terms of accuracy and efficiency. As a matter of fact, the estimated conductivities using the Refined approach feature lower  $L^2$ -norm of the error. Moreover, the use of the informed initial guess allows faster convergence of the optimization procedure as well as a huge reduction of the computational cost. Therefore, we use the Refined scheme throughout the following numerical tests.

Table 3 demonstrates that our method is accurate and efficient regardless of the amount of noise. The mean of the estimated conductivity fields accurately matches the exact conductivities. The low standard deviation implies that the estimations are smooth and consistent with the uniformity of the true conductivity. The error  $|u - u_{meas}|$ 

**Table 3** Mean and standard deviations of the estimated fields for different percentage of noise p. Uniform isotropic conductivity,  $\sigma_{l,exact}(\mathbf{x}) = \sigma_{t,exact}(\mathbf{x}) = 6 \cdot 10^{-3} \text{ cm}^2/\text{ms}$ . Here, # fwd denotes the number of solves of the state equations, and # bwd represents the number of solves of the adjoint equations. Accuracy is preserved even in case of high percentage of noise in the data.

% noise	1%		5%		10%		
	Mean	st.dev.	Mean	st.dev.	Mean	st.dev.	
$\sigma_{l,est}$	$6.0 \cdot 10^{-3}$	$3.4 \cdot 10^{-5}$	$6.0 \cdot 10^{-3}$	5.2 · 10 <sup>-5</sup>	$6.1 \cdot 10^{-3}$	5.2 · 10 <sup>-4</sup>	
$\sigma_{t,est}$	$5.9 \cdot 10^{-3}$	$1.2 \cdot 10^{-4}$	$5.9 \cdot 10^{-3}$	$1.2 \cdot 10^{-4}$	$5.9 \cdot 10^{-3}$	$9.2 \cdot 10^{-5}$	
# fwd  bwd	20	18	28	19	24	4 18	

**Table 4** Mean and standard deviations of the estimated fields for the case  $\sigma_{l,exact}(\mathbf{x}) = 4 \cdot 10^{-3} \text{ cm}^2/\text{ms}$ ,  $\sigma_{t,exact}(\mathbf{x}) = 2 \cdot 10^{-3} \text{ cm}^2/\text{ms}$ .  $\|\sigma_{l,0} - \sigma_{l,exact}\| / \|\sigma_{l,exact}\| = \|\sigma_{t,0} - \sigma_{t,exact}\| / \|\sigma_{t,exact}\| = 5 \cdot 10^{-1}$ , p = 5%. The algorithm is reliable and the estimation matches the true conductivity fields.

	$L^2$ error	Mean	st. dev.
$\sigma_{l,est} \ \sigma_{t,est}$	$7.9 \cdot 10^{-3} \\ 5.9 \cdot 10^{-2}$	$4 \cdot 10^{-3} \\ 2 \cdot 10^{-3}$	$3.2 \cdot 10^{-5} \\ 2.7 \cdot 10^{-5}$

**Table 5**  $L^2$  relative error, mean and standard deviation of the estimated fields for the case  $\sigma_{l,exact}(\mathbf{x}) = 8 \cdot 10^{-3} \text{ cm}^2/\text{ms}$ ,  $\sigma_{t,exact}(\mathbf{x}) = 2 \cdot 10^{-3} \text{ cm}^2/\text{ms}$  with different initial guesses.  $\sigma_{l,mean} = 7 \cdot 10^{-3} \text{ cm}^2/\text{ms}$ ,  $\sigma_{t,mean} = 3 \cdot 10^{-3} \text{ cm}^2/\text{ms}$ . The last two rows show that, in these cases, a good initial guess is needed to obtain an accurate estimation.

$(\sigma_{l,0},\sigma_{t,0})$	$L^2$ error $\sigma_{l,est} \sigma_{t,est}$	Mean	st. dev.
$(6.0, 1.5) \cdot 10^{-3}$	$1.5 \cdot 10^{-1}   8.4 \cdot 10^{-2}$	$6.7 \cdot 10^{-3}   1.7 \cdot 10^{-3}$	$5.1 \cdot 10^{-4}   4.2 \cdot 10^{-5}$
$(6.5, 3.5) \cdot 10^{-3}$	$1.4 \cdot 10^{-1}   1.0 \cdot 10^{-2}$	$6.8 \cdot 10^{-3}   2.0 \cdot 10^{-3}$	$1.3 \cdot 10^{-4}   2.2 \cdot 10^{-5}$
$(7.0, 3.0) \cdot 10^{-3}$	$3.4 \cdot 10^{-2}   6.0 \cdot 10^{-3}$	$7.7 \cdot 10^{-3}   2.0 \cdot 10^{-3}$	$1.7 \cdot 10^{-4}   1.8 \cdot 10^{-5}$
$(9.0, 4.0) \cdot 10^{-3}$	$1.4 \cdot 10^{-2}   4.4 \cdot 10^{-2}$	$7.9 \cdot 10^{-3}   1.9 \cdot 10^{-3}$	$1.6 \cdot 10^{-4}   5.0 \cdot 10^{-5}$

at different time steps is shown in Fig. 1(b). The discrepancy between the true and the reconstructed potential is higher nearby the wavefront, whereas it is lower and comparable to the noise level elsewhere.

### 4.2. Uniform anisotropic conductivity

In the following tests, anisotropic uniform conductivity fields are prescribed. Two anisotropy ratios are investigated,  $\sigma_l/\sigma_t = 2$  and  $\sigma_l/\sigma_t = 4$  as typical for the cardiac tissue [1]. As for the first case, we impose  $\sigma_{l,exact}(\mathbf{x}) = 4 \cdot 10^{-3} \text{ cm}^2/\text{ms}$ ,  $\sigma_{t,exact}(\mathbf{x}) = 2 \cdot 10^{-3} \text{ cm}^2/\text{ms}$ . The initial guess is  $\sigma_{l,0}(\mathbf{x}) = 2 \cdot 10^{-3} \text{ cm}^2/\text{ms}$ ,  $\sigma_{t,0}(\mathbf{x}) = 1 \cdot 10^{-3} \text{ cm}^2/\text{ms}$  and  $\sigma_{l,mean}(\mathbf{x}) = 5 \cdot 10^{-3} \text{ cm}^2/\text{ms}$ ,  $\sigma_{t,mean}(\mathbf{x}) = 3 \cdot 10^{-3} \text{ cm}^2/\text{ms}$ . The noise percentage is p = 5%. As reported in Table 4, the algorithm yields reliable estimates, with  $\sigma_{l,ext}$  featuring lower error. For the way

As reported in Table 4, the algorithm yields reliable estimates, with  $\sigma_{l,est}$  featuring lower error. For the way the numerical experiment was set up, this is reasonable, since the longitudinal direction is more informative of the dynamics of the system than the transversal one therefore the estimation of  $\sigma_l$  is expected to be more accurate. Different initial guesses were tested as well obtaining similar results.

For the second anisotropy ratio, the true conductivities are set to be  $\sigma_{l,exact}(\mathbf{x}) = 8 \cdot 10^{-3} \text{ cm}^2/\text{ms}$  and  $\sigma_{t,exact}(\mathbf{x}) = 2 \cdot 10^{-3} \text{ cm}^2/\text{ms}$ . Table 5 pinpoints the importance of the initial guess, even for the Refined scheme. With an accurate initial guess the final results are significantly accurate, particularly for the estimate of  $\sigma_l$ .

One possible reason for the high sensitivity on the initial guess in this case is that, since  $\sigma_l$  is higher, the wavefront propagation is faster, therefore the more samples are needed to be sufficiently informative of the dynamics. Therefore, the conduction velocity related to the initial guess needs to be sufficiently close to the measurements to ensure a reliable estimation of the conductivity. Ideally, a possible workaround would be lowering  $dt_{snap}$ , for instance

by setting  $dt_{snap} = 1$  ms, so that more data are involved in the minimization. However, we chose not to investigate this solution because it is not feasible in an experimental setting. As a matter of fact, the temporal resolution of the optical camera used to record AP measurements *in vitro* experiments is usually 2 ms [28,45].

#### 4.3. Presence of a scar

We now focus on the estimation of conductivities in a pathological tissue. In the following test, the cardiac tissue is scarred, that means that a portion of the tissue has an abnormal value of the conductivities. Detection of anomalies based on a similar variational approach to the one advocated here is considered in recent works [46–48]. The presence of a scar on real patients may trigger pathological patterns in the action potential propagation. Here, the scar is represented (Fig. 2(a)) as a circular region with radius 1.5 cm located at the center of the tissue featuring the anomalous values of conductivities [49].

As shown in Fig. 2(b), the optimization procedure is able to detect correctly both the location of the scar and the conductivity values. The initial guess in Fig. 2(c) features a discontinuity on the tissue and this is a reasonable choice since the presence of a scar can be visually detected by looking at the data. However, the algorithm has been also tested starting from uniform conductivities and it provides similar results. The error  $|u - u_{meas}|$  with the respect to the dynamics shown in Fig. 2(d) at different time steps is shown in Fig. 2(e). The downside of our methodology in this case is that the computational burden substantially increases due to significant growth of the number of optimization iterations. The estimation process needs 132 forward solves and 58 backward solves, that means a huge increment with respect to the uniform case. This reflects on higher computation time, as it increases from 20 h of the uniform case to roughly 70 h. This motivates further studies in model order reduction approaches for a more efficient solution as in [29].

#### 4.4. Canine tissue geometry

Moving towards the validation with experimental data, we test the accuracy of the estimation procedure considering a realistic geometry of a portion of a canine ventricular tissue [28]. 2D simulations are performed as the optical mapping data used for experimental validation consist of voltage recordings on a 2D grid. First of all, we need to assess an accurate resolution for the fine mesh used for modeling the transmembrane potential u so that the CV of the real wavefront propagation can be accurately reproduced. It is well-known from the literature that coarse meshes lead to overestimation of the CV [50–52]. Therefore, the mesh must be fine enough to accurately catch the physics of the problem. A reasonable level of discretization can be identified by looking at the plateau point of the CV convergence plot. Such a plot is obtained by estimating the CV in some points of the mesh at different resolutions h, the maximum diameter of the mesh. Below a certain threshold on h, the CV remains constant meaning that the mesh is fine enough to reliably describe the dynamics of the system. Using fine meshes clearly increases the computational costs. This can be mitigated by resorting to non-conforming finite elements recently discussed in the literature [53].

From Fig. 3, we notice that for any h < 0.03 cm, the CV at three aligned points of the mesh remains constant, so we argue that  $\bar{h} = 0.03$  cm is the minimum resolution of the mesh that guarantees an accurate approximation of the physics of the problem. Following this rationale, we chose h = 0.028 cm (corresponding to about 120k DOFs) which is a good trade-off between accuracy of the simulation and computational costs. The number of DOFs of the coarse mesh for the discretization of the conductivities is 99. Fig. 4(a) shows the cardiac fiber structure that was roughly approximated by looking at anatomy of the tissue. The stimulus is applied at the top of the domain for a duration of 2 ms. The potential propagation at different time steps for the case  $\sigma_{l,exact}(\mathbf{x}) = 7 \cdot 10^{-3}$  cm<sup>2</sup>/ms,  $\sigma_{t,exact}(\mathbf{x}) = 2 \cdot 10^{-3}$  cm<sup>2</sup>/ms is shown in Fig. 4(b). Gaussian noise with p = 5% was added to the synthetic data and  $\sigma_{l,mean}(\mathbf{x}) = 6 \cdot 10^{-3}$  cm<sup>2</sup>/ms,  $\sigma_{t,mean}(\mathbf{x}) = 3 \cdot 10^{-3}$  cm<sup>2</sup>/ms.

Several anisotropy ratios are chosen to test the estimation procedure as shown in Table 6. In each case, the algorithm is able to accurately retrieve the true conductivity fields. As for the sensitivity to the initial guess, when the CV is slow, the method is robust with respect to the choice of  $(\sigma_{l,0}, \sigma_{t,0})$ . On the other hand, for the cases with faster CV, the initial guess has to be carefully selected to guarantee a reasonable accuracy, as discussed in the previous section. These simulations were more computationally demanding than the tests on the square domain (approximately 30 h vs. 20 h of the square cases) because of the finer mesh resolution.

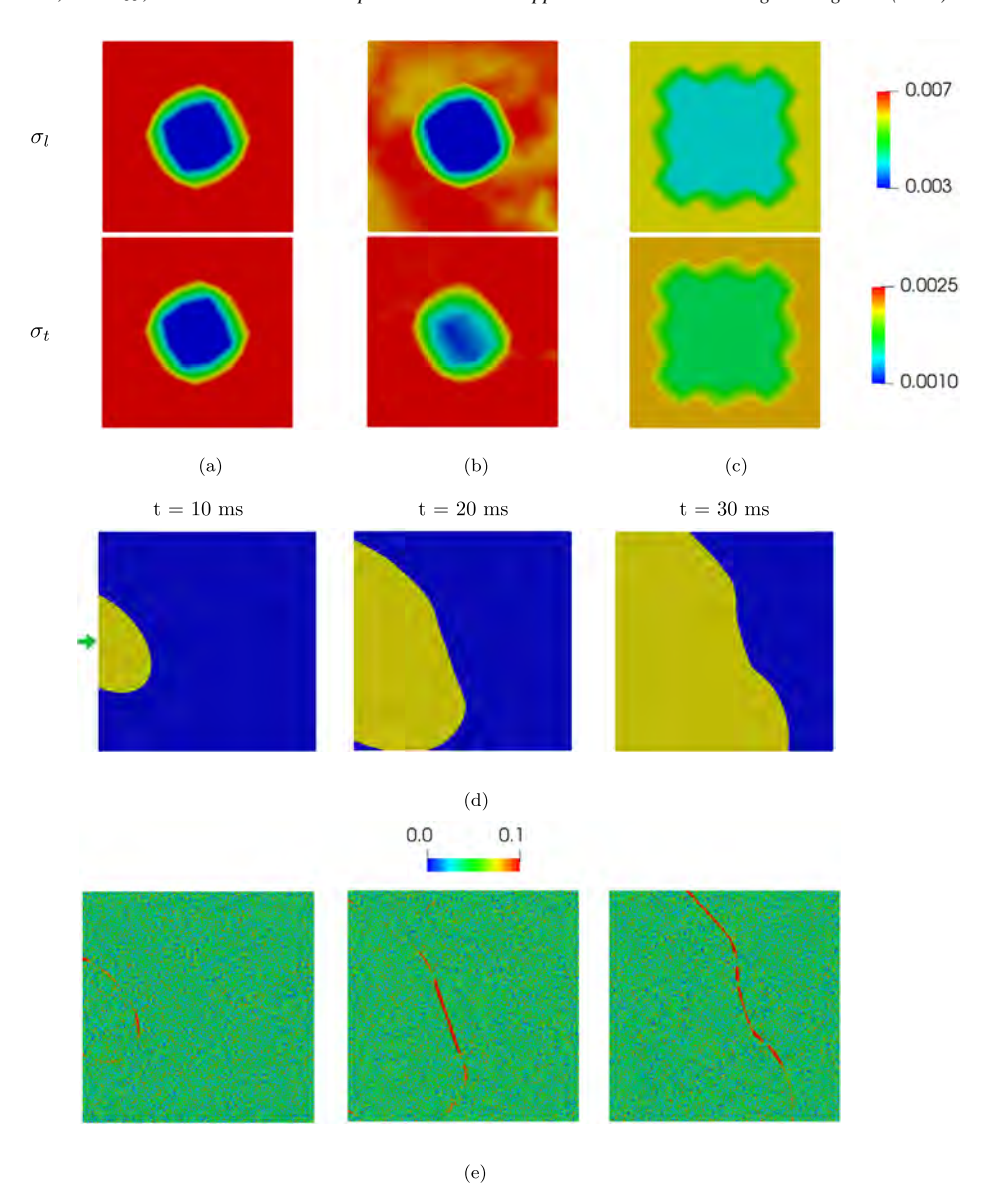


Fig. 2. (a) Pathological tissue with a circular scar in the center featuring lower conductivity. (b) Estimated conductivity fields. (c) Initial guess. (d) Synthetic AP propagation in presence of the scar. The wavefront slows down in the scar because of lower conductivity in that region. Green arrow indicates the site of stimulation. (e)  $|u - u_{meas}|$  at different time steps.

Table 6  $L^2$  relative error, mean and standard deviation of the estimated conductivity fields [cm<sup>2</sup>/ms] in different cases for canine ventricular tissue geometry. The optimization procedure provides a reliable reconstruction of the true conductivity fields. In the last two cases featuring a faster CV, the accuracy of the estimation depends more significantly on the quality of the initial guess, as already shown in Table 5.

$(\sigma_{l,exact},\sigma_{t,exact})$	L2 error $\sigma_{l,est} \sigma_{t,est}$	Mean	st. dev.
$(5.0, 2.0) \cdot 10^{-3}$	$3.6 \cdot 10^{-2}   2.6 \cdot 10^{-2}$	$4.8 \cdot 10^{-3}   2.0 \cdot 10^{-3}$	$3.1 \cdot 10^{-4}   3.9 \cdot 10^{-5}$
$(6.0, 1.5) \cdot 10^{-3}$	$3.7 \cdot 10^{-2}   2.3 \cdot 10^{-2}$	$5.8 \cdot 10^{-3}   1.4 \cdot 10^{-3}$	$3.1 \cdot 10^{-4}   4.3 \cdot 10^{-5}$
$(7.0, 2.0) \cdot 10^{-3}$	$4.6 \cdot 10^{-2}   3.1 \cdot 10^{-2}$	$6.8 \cdot 10^{-3}   2.1 \cdot 10^{-3}$	$8.7 \cdot 10^{-4}   5.1 \cdot 10^{-5}$
$(10.0, 3.0) \cdot 10^{-3}$	$4.4 \cdot 10^{-2}   3.2 \cdot 10^{-2}$	$9.8 \cdot 10^{-3}   3.1 \cdot 10^{-3}$	$7.9 \cdot 10^{-4}   4.4 \cdot 10^{-5}$

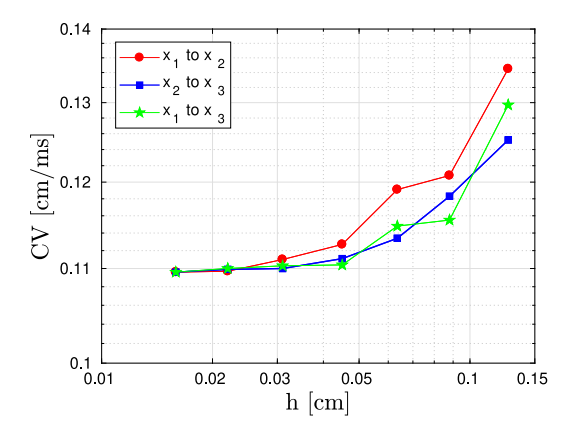


Fig. 3. CV convergence plot at different resolutions h in three aligned points of the mesh. Any resolution h < 0.03 cm provides a reliable approximation of the physics of the system.

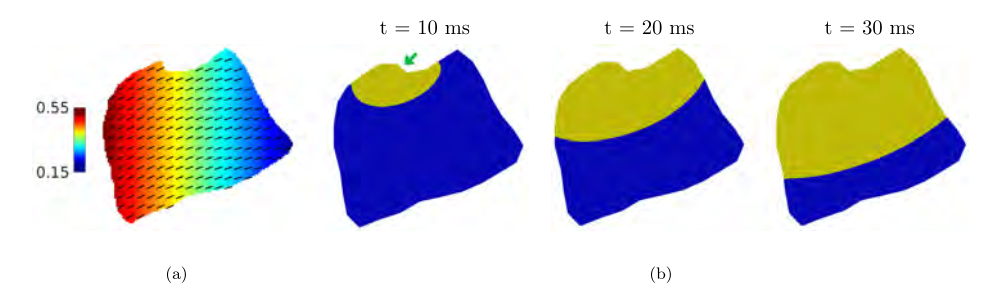
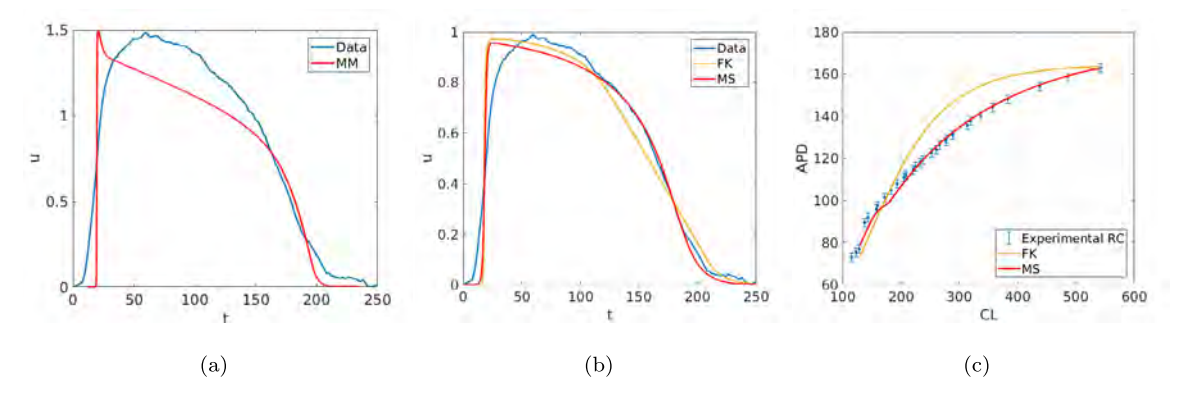


Fig. 4. (a) Realistic geometry of a portion of a canine ventricular tissue and approximation of the fiber structure. The segments represent the local cardiac fiber direction and the colorbar indicates the value of the local fiber angle with respect to the x-axis. Unit is in radians. (b) Three snapshots of  $u_{meas}$  (contour line  $u_{meas} = 0.75$ ). Green arrow indicates the site of stimulation where AP is triggered propagating towards the bottom.

### 5. Validation with experimental data

Fluorescence optical data. Fluorescence optical mapping recordings were obtained from canine right ventricle wedge preparations, according to the experimental protocols approved by the Institutional Animal Care and Use Committee of the Center for Animal Resources and Education at Cornell University. We refer to [22,28] for details of the experimental setup. The imaging has a spatial resolution of  $\sim 600 \, \mu m$  per pixel for a grid size of  $\sim 7 \times 7 \, cm^2$ and a temporal resolution of 2 ms. Data filtering and postprocessing were performed via a custom-built interactive Java program, in particular for removing signal drift and fluorescence noise, normalizing the signal on a pixelby-pixel basis, averaging in time on a 7 frames length, and averaging in space with a two-dimensional weighted Gaussian function. The resulting analyzed data have been proved to retain tissue local heterogeneities, amenable for an extensive usage for modeling purposes [54–57]. For estimating space-dependent cardiac conductivities from action potential data obtained at different pacing Cycle Length (CL), we tuned the ionic model parameters to fit the APD-RC. The experimental APD-RC was obtained by applying multiple electrical stimulations, e.g. 20, at constant pacing with period CL starting from high values (typically 1000 ms) and decreasing in 50 ms steps until reaching CL = 250 ms, after which CL was shortened in 10 ms decrements until capture was lost or ventricular fibrillation was induced. At each CL, pacing was applied for at least 1 min before recording to ensure that steady state was reached, then recordings were made for 5 s, or more, at each CL. APD was measured at 25% repolarization threshold ensuring a minimum level of basal noise. The RC is then obtained by plotting APD vs. CL.

Choice of the ionic models. As we refer to canine experimental data, we needed to calibrate the ionic model accordingly. The MM used in the synthetic validation does not fit at best the available experimental data, since the temporal resolution of the optical mapping camera used for data collection is not fine enough to catch the upstroke of the action potential. This results in a much smoother AP shape (see Fig. 5(a)). Therefore, although the MM



**Fig. 5.** (a) AP shape modeled with the Minimal model. The AP features an upstroke that is missing in the experimental data. (b) Simulated AP shapes for FK and MS. Red curve represents the modeled AP and the blue the experimental one. MS provides a better match than FK especially in the repolarization phase. (c) Experimental APD restitution curve compared with the modeled ones obtained with MS and FK models.

model provides a realistic simulation of cellular electrical activity, we considered the FK and MS models instead. Even though these models provide a much more simplified approximation of the physics of the problem, they are expected to provide a better reconstruction of the data at hand because of the AP shape similarity with optical data.

The model-based restitution curves were calculated performing one dimensional cable simulations and following a protocol similar to the experimental one. The ionic model parameters were manually tuned so to minimize the discrepancy between experimental and the modeled restitution curves. The AP shapes and restitution curves for the FK and MS ionic models are shown in Figs. 5(b), and 5(c), respectively. It is worth noting that, for the single case of experimental data we are considering, the MS model yields a better fit of the experimental RC than the FK one, especially at high CL, as well as a more accurate match of the AP shape. On the other hand, FK features a more realistic wavefront propagation at low CL, as we will see in the following tests. The 2D fine mesh for approximating u has the maximum diameter h = 0.028, T = 230 ms,  $dt_{snap} = 2$  ms and  $\alpha_0 = \alpha_1 = 0$ . As for computation time, depending on the ionic model and the values of CL, the following tests took on average between 2 and 5 h on XSEDE Stampede II facilities.<sup>1</sup>

#### 5.1. Validation at slow pacing rates

We estimated the conductivities from AP optical mapping measurements recorded at CL = 540 ms. Three different resolutions h = (1, 0.44, 0.25) cm are considered for the coarse mesh. The aim was determining the minimum resolution in order to capture enough heterogeneity in the conductivity fields and, in turns, to be able to provide an accurate reconstruction of the experimental data. For each resolution, conductivity fields are estimated using the FK model. The initial guess of the optimization algorithm was chosen such that the wavefront propagation is comparable to the experimental data.

As shown in Fig. 6(a), the estimation highly depends on the mesh. In particular, a significant discrepancy can be observed between the results obtained with h = 1 cm and h < 1 cm. The conductivity maps look similar for h = 0.44 cm and h = 0.25 cm. Henceforth, we used the coarse mesh with h = 0.44 (# DOFs = 512) cm to limit computational costs. The conductivity fields obtained with the MS model shown in Fig. 6(b) are comparable—though varying over a wider range—to the ones retrieved with the FK one in Fig. 6(a), meaning that the two models are able to detect both fast and slow conducting regions. In addition, we tested the assumption of anisotropic conductivities by comparing the results with the reconstruction obtained assuming isotropic conductivities ( $\sigma_l = \sigma_t$ ) (displayed in Fig. 7).

Fig. 7 shows a comparison between the contours line at u = 0.5 of the experimental data and the modeled AP propagation using MS and FK models with anisotropic conductivity and FK model with isotropic conductivity

<sup>&</sup>lt;sup>1</sup> A direct comparison of computational time between synthetic and real data test cases is not possible, as we used different facilities. We devoted the High Performance Computing facilities of Stampede II only for the most important real-data validation.

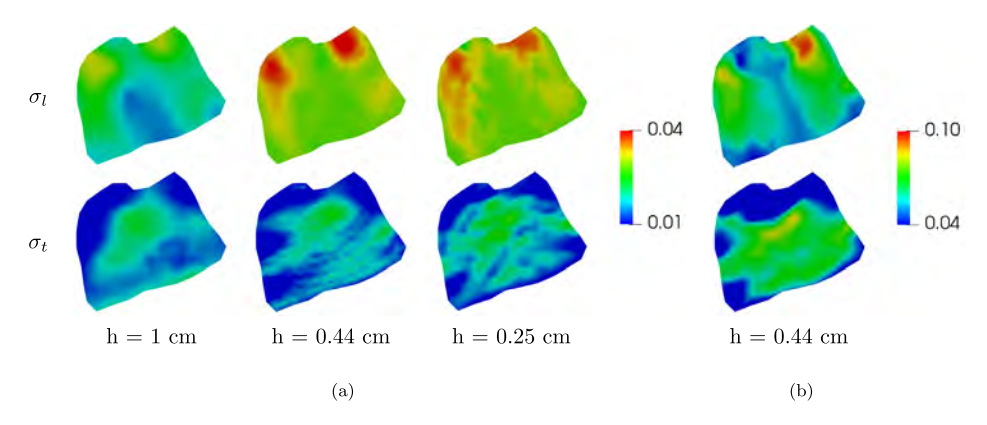


**Fig. 6.** Estimated conductivity fields at CL = 540 ms: (a) FK model with three levels of discretization of the coarse mesh; (b) MS model. While there is a huge difference between the estimations at h = 1 cm and h = 0.44 cm, the results at h = 0.44 and h = 0.25 cm are qualitatively similar. Therefore, we select the coarse mesh with h = 0.44 cm to perform experimental validation. Moreover, MS and FK models identify similar slow and fast conducting areas.

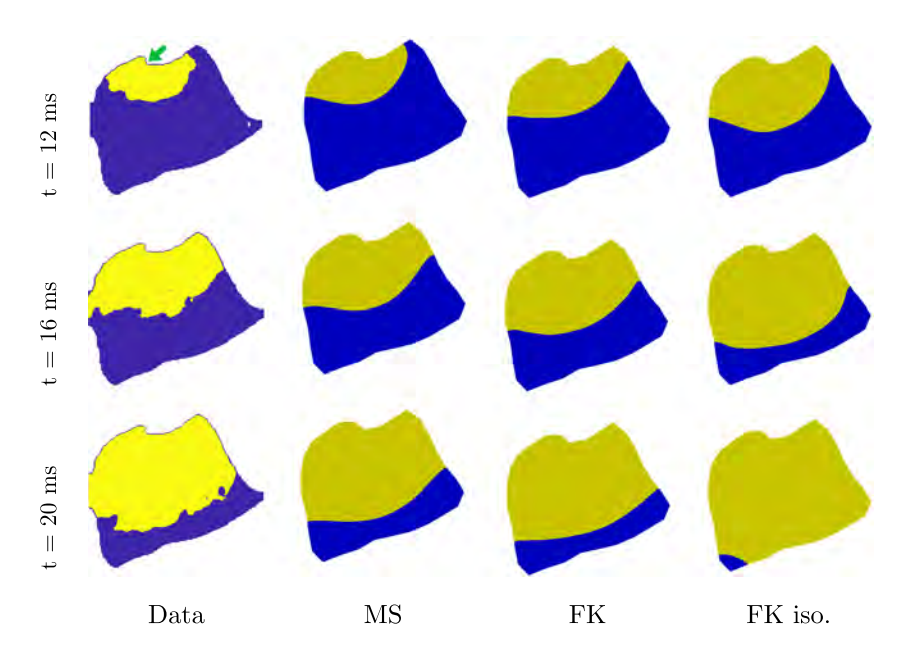


Fig. 7. CL = 540 ms, comparison between experimental and modeled contour lines assuming anisotropic (MS and FK) and isotropic conductivity fields (FK iso.). Green arrow indicates the site of the stimulation. The lack of anisotropy in the conductivity leads to a poor reconstruction of the experimental data.

at three snapshots. Regardless of the ionic model, the reconstruction of experimental data seems accurate both in shape of the wavefront and its velocity for t=16 ms and t=20 ms. As for t=12 ms, the algorithm coupled with the FK model overestimates the conductivity in the region near the stimulation point leading to a higher CV. On the other hand, the MS outperforms FK providing a more reasonable reconstruction of the wavefront propagation. Moreover, the estimation comes along with less computational effort since the MS model is much simpler and faster to solve than FK. Therefore, MS is preferable to FK both in terms of accuracy and reduction of the computational costs. However, for lower values of CL at which the dynamics of the system become more challenging to model, we may expect FK to perform better than MS since it provides a more accurate approximation of the physics of the problem.

Nevertheless, since the measurement errors are higher in proximity of the stimulation point and the data are more noisy, we will only focus on the modeled AP propagation sufficiently far away from the stimulation area in

order to provide a fair comparison between the estimates. It is also noticeable that the assumption of anisotropic conductivities is crucial for the accurate reconstruction of the real data. As a matter of fact, assuming isotropic conductivity leads to poor reconstruction of the experimental data since the CV is overestimated at each snapshots. This might be due to the fact that the isotropic conductivity does not take into account the effect of the fibers on the propagation of the electrical signal which however is crucial for an accurate reconstruction of the real AP. Henceforth, we consider anisotropic conductivities only.

# 5.2. The role of CL on the estimation

In the following numerical tests we investigate the interplay between the reliability of our estimation procedure and the value of CL. The conductivity fields are estimated using data collected at decreasing values of CL retrieved from the experimental APD restitution curve. For each value of CL, we consider two different strategies for initializing the optimization algorithm.

The first strategy is using the estimation of  $\sigma$  obtained at the previous CL as an initial guess for the next inverse problem. We call this a *dynamic* procedure, as it combines the experimental observations with a prior knowledge in order to initialize the optimization algorithm. The second approach, called *static*, consists of using the same initial guess  $\sigma_0$  for all the parameter identifications performed at each value of CL. A uniform isotropic conductivity field of value 0.01 cm<sup>2</sup>/ms (used to fit the experimental APD restitution curve) is chosen as initial guess.

The dynamic approach is expected to outperform the static one because the optimization algorithm starts from an initial guess already providing a reliable match of the data. Moreover, setting realistic initial condition  $u_0(\mathbf{x})$  for the forward solver is crucial for an accurate simulation of the electrical propagation, especially at low CL. As a matter of fact, numerical experiments have shown that pacing of resting cardiac tissue ( $u_0(\mathbf{x}) = 0$ ) at low CL does not trigger AP propagation. Therefore,  $u_0(\mathbf{x})$  is set following a protocol similar to the experimental one. The tissue is electrically stimulated twice starting from high CL (typically 500 ms or higher) and decreasing in 50 ms decrements until reaching 300 ms, after which the CL is shortened in 20 ms decrements. Once the desired CL is reached, pacing is applied twice and the final state is stored and used as initial condition for the forward solve in the estimation process. By following this strategy, the system responds to stimuli even at low CL and electrical wave propagation is triggered.

Here, we report the results of the estimation for decreasing values of CL = [540, 357, 289, 233] ms. The estimated conductivity fields for different CL values and strategies using the MS model are shown in Figs. 8(a) and 8(b).

Looking at the misfit  $\mathcal{J}$  with MS and the dynamic vs. the static strategy (see Fig. 9, bottom), the former provides a more accurate reconstruction of the experimental data and has therefore to be preferred. However, both the strategies coupled with the MS model perform poorly as CL decreases resulting in an increase of the misfit. As MS aims at simulating only the basic characteristics of the action potential, we get an overly simplified approximation of the dynamics, especially at low values of CL. Moreover, since it features only one gating variable, MS is not able to reliably reproduce the behavior of the system at fast pacing. This results in an underestimation of the conduction velocity. As noticed in Fig. 9, top, the potential propagation is much slower than the real data at low CL. This is further highlighted by Fig. 10 which compares the experimental and modeled APs obtained with the two different procedures and ionic models in one point on the tissue in the time window [0, 250] ms. The delay of the modeled AP is evident especially in the case CL = 233 ms when using MS model, regardless of the strategy. Moreover, the peak of the AP markedly decreases at low CL, in particular in the static procedure, contributing to the increase of the functional  $\mathcal{J}$ .

More realistic results can be obtained when using the FK model. At high CL, the estimation features slightly larger misfit than the dynamic strategy with MS model because of the better reconstruction of the AP shape provided by MS (see Fig. 9, bottom). However, the strategy performs much better at low CL, in particular when CL < 300 ms, as the misfit functional remains stable. Despite the improvement of the reconstruction, the results are still not fully satisfying since the conduction velocity is now overestimated leading to an increase of the conductivity, especially at low CL (see Fig. 11(a)). This is highlighted in Fig. 10 too in which the AP simulated with FK at CL = 233 ms precedes the experimental data meaning that the wavefront propagation is faster. This disagrees with the physics of the system because it has been noticed in the experimental setting that the conduction velocity decreases as CL decreases. We argue that this can be caused by the high measurement errors nearby the stimulation point that are

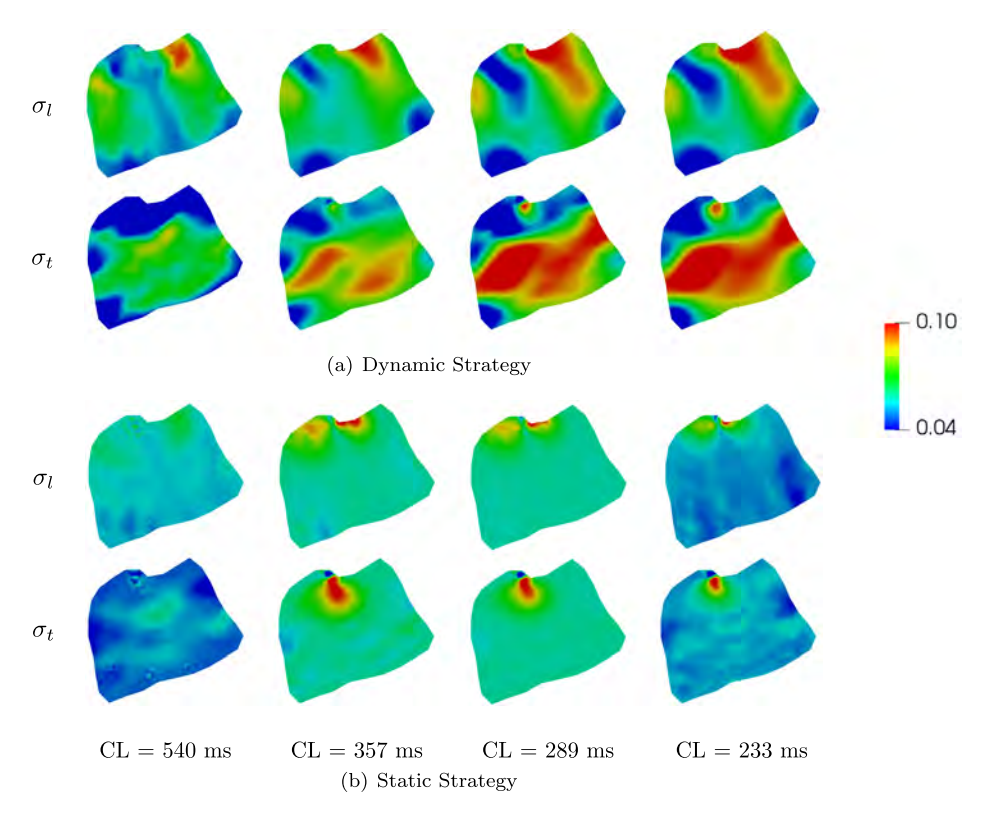


Fig. 8. (a) Dynamic Strategy, (b) Static strategy: estimated conductivity fields with MS model. These results pinpoint how an educated selection of the initial guess is critical for the reliability of the estimation.

detrimental to the accuracy of the estimation process, in particular at low CL. It is worth noting that the optimization procedure was done with no regularization, so the presence of these errors may affect significantly the quality of the estimation. To overcome this issue, we enable the Tikhonov-like regularization term minimizing the mismatch between the estimated conductivity and mean value only in proximity of the stimulation point (see Appendix). In particular, we impose  $\sigma_{l,mean}(\mathbf{x}) = 9 \cdot 10^{-3} \text{ cm}^2/\text{ms}$ ,  $\sigma_{t,mean}(\mathbf{x}) = 3 \cdot 10^{-3} \text{ cm}^2/\text{ms}$  with  $\alpha_2 = 10^{-2}$  in a small region around the stimulation point and  $\alpha_2 = 0$  elsewhere. These values of mean conductivities were manually tuned to replicate an AP propagation comparable to the experimental one nearby the stimulation point. The value of  $\alpha_2$  was chosen to enforce the estimates to be close to the prescribed mean value only in the area by the site of the stimulation, whereas the regularization is not needed so it is disabled elsewhere.

This strategy yields a more accurate estimation, in particular at low CL, resulting in lower misfit value (see Fig. 9, bottom). Moreover, as it can be noticed in Fig. 9, top, the reconstruction of the data is more reliable in terms of the conduction velocity as well, since the modeled AP propagation is similar to the experimental one. It is also important noting from the shape of the contour line that the curvature of the wavefront varies along the tissue meaning that the procedure is able to detect the heterogeneity of the conductivity. Finally, the estimations of the conductivity fields reported in Fig. 11(b) are in agreement with the CV reduction at small CL as observed in the experiments.

#### 6. Conclusions

The estimation of the cardiac conductivities is an old problem [10,12,13], reinvigorated by mathematical modeling and data assimilation techniques [15,19,20,29,58]. As numerical simulations are progressively becoming part of medical research and clinical practice, an accurate parameter estimation is critical, possibly to customize models to patient-specific settings. The data-assimilation framework combining available measures with accurate models allows the successful accomplishment of this task. In fact, there are several possible approaches, ranging

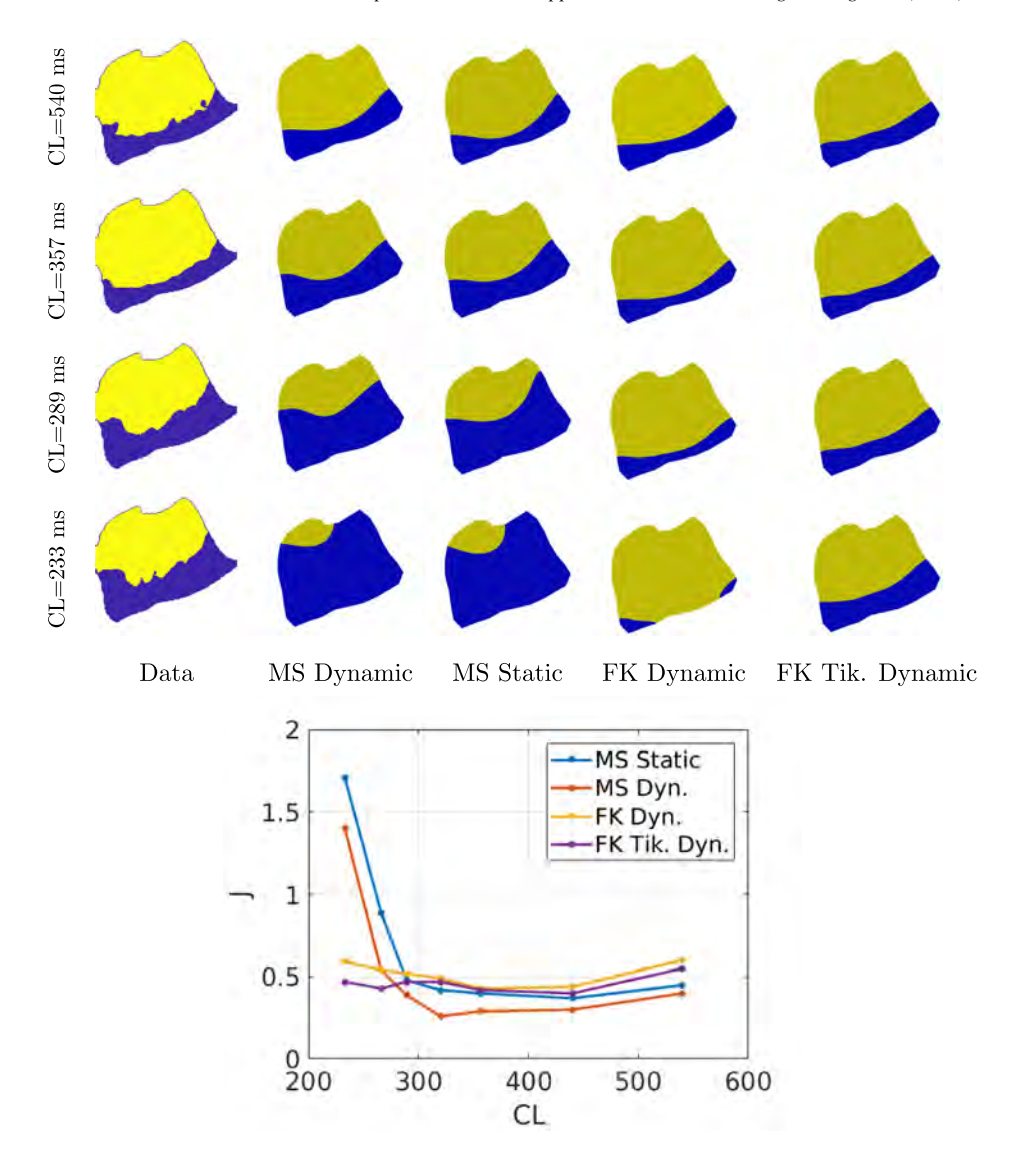
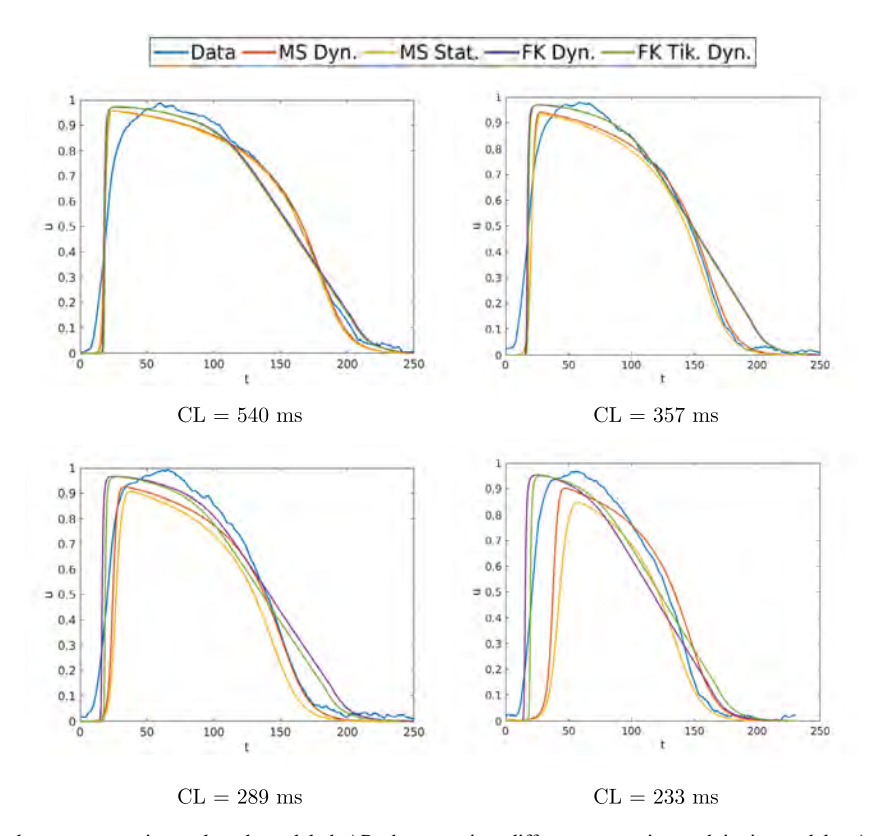


Fig. 9. Top: Comparison between experimental and modeled contour line u = 0.5 at t = 20 ms for different CL. At low CL, dynamic and static strategies with MS model underestimate the experimental CV, whereas dynamic approach with FK model simulates faster AP propagation. Enabling the Tikhonov-like regularization term allows us to provide a reasonable match of the experimental data at low CL. Bottom: Value of misfit J for the different numerical settings tested. At fast pacing rates (low CL), both dynamic and static strategies with MS model (red and blue curve, respectively) lose accuracy as the misfit increases. By using the dynamic approach with FK model (orange curve), we can provide a better match of the experimental data. However, the reconstruction of the real AP propagation is still unsatisfactory (see Fig. 9, top). The dynamic technique with FK model and Tikhonov-like regularization is the best strategy both in terms of misfit and reconstruction of the data.

from stochastic procedures (Kalman filtering) to deterministic techniques. We have developed in the last years a variational methodology based on the Lagrange multiplier approach [20,29], that was previously tested in fully synthetic benchmarks [15]. Since real settings may significantly differ from purely numerical test, we performed here an extensive validation of the procedure with experimental data. Precisely, we tested our method with optical AP measurements. By performing a large numerical campaign, we proved that the optimization algorithm is reliable and able to retrieve the conductivity fields. Then, we validated the procedure using fluorescence optical mapping recordings at different pacings. After a careful selection of the modeling and numerical setting, we showed that the



**Fig. 10.** Comparison between experimental and modeled AP shapes using different strategies and ionic models. At low CL, the results obtained with MS model clearly diverge from the real data, both in terms of wavefront propagation and magnitude of the peak of the AP. FK model coupled with Tikhonov-like regularization in the dynamic framework gives the most reliable reconstruction of the experimental wavefront propagation.

method successfully reproduces most of the dynamics obtained from the experiments providing reasonable estimates of conductivity fields that are consistent with the data.

When modeling the electrophysiology and, specifically, setting up reliable parameter estimation procedures based on data, we have no silver bullet. The variety of options and modeling choices is huge and, generally, depends on the specific aims and regimes considered. The computational costs and the overall effectiveness of our estimation procedure are significantly affected by these choices, so the identification of the most convenient trade-offs is generally not easy. Also, it is worth mentioning that the setting-up of computationally efficient methods is still an active research field, and the current scenario will likely change in the future [25,26,53,59–64] (to mention a few contributions).

In this paper, we focus on the Monodomain model with the MS and the FK models. The Monodomain model was justified in previous papers, as a trade-off between computational costs and effectiveness of the estimated conductivities [20]. The ionic models selected guarantee a relatively high reliability in spite of the low number of parameters they feature. In our variational parameter estimation procedure we demonstrate in this paper how their choice may be dictated by the CL pacing. While MS works properly over a wide range of CL pacing, at low frequency, FK performs better.

A reliable and efficient estimation of cardiac conductivity for patient-specific modeling is turn for using optimization techniques in the therapy of cardiac disorders related to the potential propagation [6–8]. Our ultimate goal, in fact, is the combination of data assimilation techniques and optimization procedures for improving the clinical activity. An extensive testing against experimental data is a fundamental step in this perspective to certify the credibility of the approach.

Several improvements are still to be done. The tuning of the parameters and the initial guess for the nonlinear iterations is at this stage mostly empirical, even if we presented some approaches that improve the performances

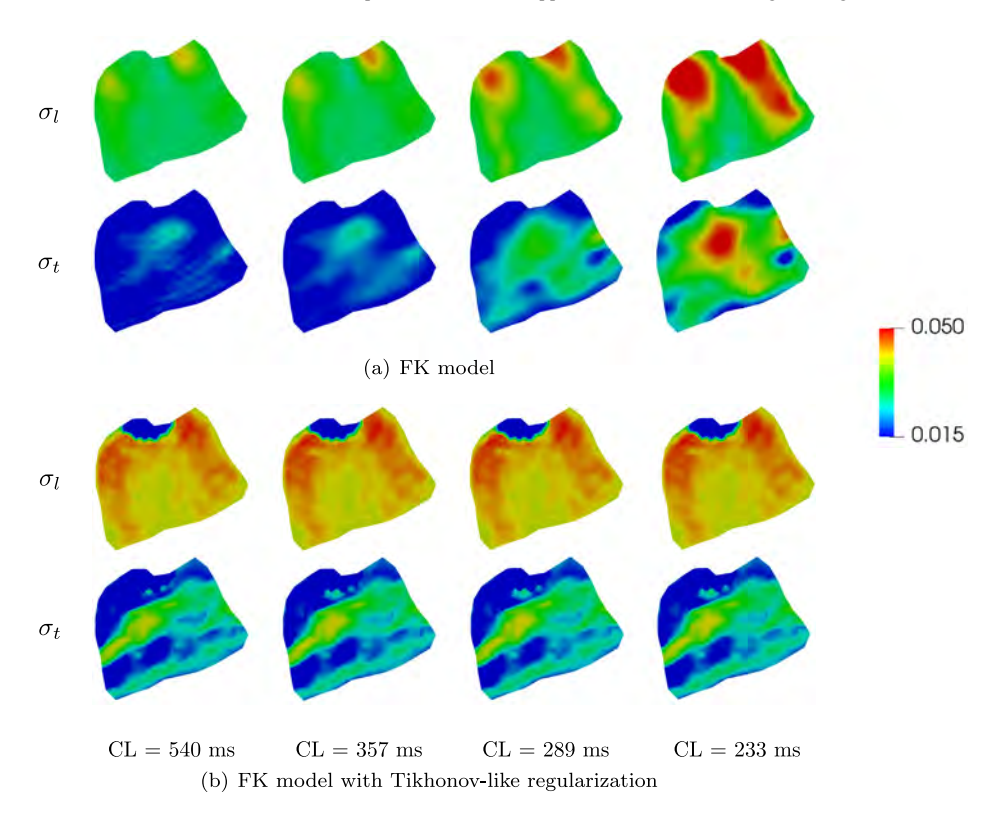


Fig. 11. Dynamic Strategy: estimated conductivity fields with (a) FK model and (b) Tikhonov-like regularization. The conductivities estimated in (a) increase at low CL. This lacks physical foundation because it has been noticed in the experiments that the CV (and so the conductivity) decreases at low CL. On the other hand, the results obtained in (b) are more in line with the experimental expectation as the magnitude of the estimated fields does not increase at low CL.

by a smart preprocessing of the arbitrary initial guess of the conductivities. Strategies for an automatic tuning of these parameters are an interesting practical follow-up of the present work. Moreover, as pointed out above, several parameters beyond the conductivities need to be estimated. The ionic-model parameters, dependent on the local natural heterogeneities of the cardiac tissue, as well as the fiber orientation, that in this paper we tuned empirically, may be estimated within a unified variational framework [19], even if this is currently too demanding from the computational point of view for a real application requiring the adoption of more involved physiological models. Moreover, we aim at including the modeling of electrical properties of the border zone (BZ) around a scar. Our methodology might be helpful to investigate and better understand the potential role of BZ in arrhythmogenesis [65,66]

We plan to extend the proposed methodology to synchronous endocardial and epicardial recordings, e.g. the one provided in [28], such to estimate the intramural conductivity and ionic parameters, eventually, that is, at present, not measurable from state-of-the-art experimental techniques. Similarly, estimation and assimilation of conductivity along repetitive fast pacing stimulations are foreseen of great potential for complex spatio-temporal alternans predictions based on statistical correlation measures [67]. On the same direction, the methodology can be applied to the cellular scale by using fluorescence optical data of calcium imaging [68,69] focusing on estimating QT syndrome related parameters [70]. In a multiphysics generalization of the present approach, we also aim at estimating temperature-dependent parameters, such as gating time constants [54,71], or dispersive modeling approaches [57,62,72,73] in which additional diffusivity parameters necessitate a rigorous experimental-based estimation.

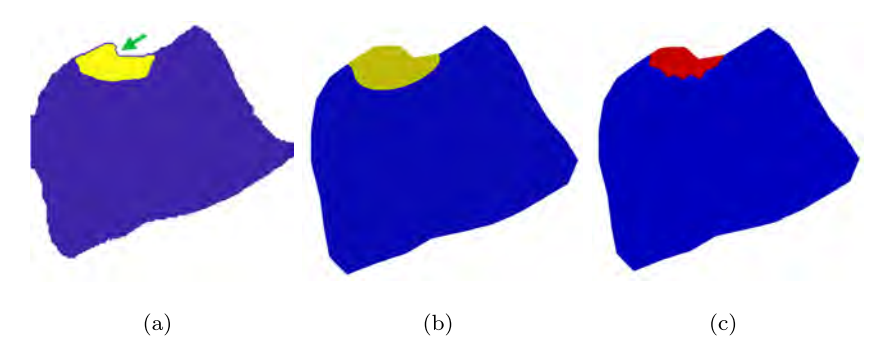


Fig. A.12. (a) Experimental AP at t = 8 ms for CL = 540 ms (contour line u = 0.5). The site of the stimulation is indicated by the green arrow. (b) Modeled AP propagation at t = 8 ms for  $\sigma_{l,mean}(\mathbf{x}) = 9 \cdot 10^{-3}$  cm<sup>2</sup>/ms,  $\sigma_{r,mean}(\mathbf{x}) = 3 \cdot 10^{-3}$  cm<sup>2</sup>/ms (contour line u = 0.5). (c) The red area surrounding the site of the stimulation is the region in which the Tikhonov-like regularization on the mean conductivity fields is imposed and  $\alpha_2 = 10^{-2}$ , whereas  $\alpha_2 = 0$  in the rest of the domain. (For interpretation of the references to color in this figure legend, the reader is referred to the web version of this article.)

# Acknowledgments

This work has been supported by the National Science Foundation — NSF, USA DMS 1412973/DMS 1413037 and the XSEDE Consortium, USA, Grant TG-ASC160069. AG and SF are grateful to the Italian GNFM-INdAM for partial supporting this work. FF is grateful to the National Science Foundation — NSF, USA DMS 1762553.

# Appendix. Tikhonov regularization

Optical mapping data is affected by experimental errors, especially in proximity of the stimulation point. This is due both to the fluorescence noise and the lack of precise information about the location of the stimulator. Therefore, the estimation procedure might be more prone to lead to an inaccurate quantification of the conductivity fields, in particular in the region surrounding the site of the stimulation. To alleviate the negative impact of measurements errors on the reliability of the reconstruction, the strategy we followed was to identify with a trial-and-error process a reasonable estimation of the conductivity fields generating an AP propagation similar to the experimental one in proximity of the stimulation point. The resulted conductivities are then enforced in the area by the stimulation point by enabling the Tikhonov-like regularization on mean conductivity values shown in (13).

We considered the time window [0,8] ms in which the voltage wave is still close to the site of the stimulation. The contour line u = 0.5 of the experimental data at t = 8 ms is shown in Fig. A.12(a). Several conductivity fields and anisotropy ratios were tested and we finally impose  $\sigma_{l,mean}(\mathbf{x}) = 9 \cdot 10^{-3}$  cm<sup>2</sup>/ms,  $\sigma_{t,mean}(\mathbf{x}) = 3 \cdot 10^{-3}$  cm<sup>2</sup>/ms. Fig. A.12(b) shows the modeled voltage wave at t = 8 ms. The region in which the Tikhonov-like regularization is imposed is represented by the red region in Fig. A.12(c). The shape of the area was chosen to be similar to the curvature of the wavefront of the experimental data. In the rest of the domain colored in blue, the regularization is disabled, so to let the estimation procedure detect the best match with the data.

### References

- [1] A.J. Pullan, L.K. Cheng, M.L. Buist, Mathematically Modelling the Electrical Activity of the Heart: from Cell to Body Surface and Back Again, World Scientific Publishing Company, 2005.
- [2] J. Sundnes, G.T. Lines, X. Cai, B.F. Nielsen, K.-A. Mardal, A. Tveito, Computing the Electrical Activity in the Heart, Vol. 1, Springer Science & Business Media, 2007.
- [3] N.A. Trayanova, Whole-heart modeling: applications to cardiac electrophysiology and electromechanics, Circ. Res. 108 (1) (2011) 113–128.
- [4] R.H. Clayton, et al., Models of cardiac tissue electrophysiology: progress, challenges and open questions, Prog. Biophys. Mol. Biol. 104 (2011) 22–48.
- [5] M. Boulakia, S. Cazeau, M.A. Fernández, J.-F. Gerbeau, N. Zemzemi, Mathematical modeling of electrocardiograms: a numerical study, Ann. Biomed. Eng. 38 (3) (2010) 1071–1097.
- [6] K. Kunisch, M. Wagner, Optimal control of the bidomain system (i): The monodomain approximation with the rogers–mcculloch model, Nonlinear Anal. RWA 13 (4) (2012) 1525–1550.

- [7] N. Chamakuri, K. Kunisch, G. Plank, On boundary stimulation and optimal boundary control of the bidomain equations, Math. Biosci. 245 (2) (2013) 206–215.
- [8] C. Nagaiah, K. Kunisch, G. Plank, Optimal control approach to termination of re-entry waves in cardiac electrophysiology, J. Math. Biol. 67 (2) (2013) 359–388.
- [9] A. Veneziani, C. Vergara, Inverse problems in cardiovascular mathematics: toward patient-specific data assimilation and optimization, Int. J. Numer. Methods Biomed. Eng. 29 (7) (2013) 723–725.
- [10] D.B. Geselowitz, An application of electrocardiographic lead theory to impedance plethysmography, IEEE Trans. Biomed. Eng. 18 (1) (1971) 38–41.
- [11] L. Clerc, Directional differences of impulse spread in trabecular muscle from mammalian heart., J. Physiol. 255 (2) (1976) 335-346.
- [12] D.E. Roberts, L.T. Hersh, A.M. Scher, Influence of cardiac fiber orientation on wavefront voltage, conduction velocity, and tissue resistivity in the dog., Circ. Res. 44 (5) (1979) 701–712.
- [13] D.E. Roberts, A.M. Scher, Effect of tissue anisotropy on extracellular potential fields in canine myocardium in situ., Circ. Res. 50 (3) (1982) 342–351.
- [14] P.R. Johnston, A sensitivity study of conductivity values in the passive bidomain equation, Math. Biosci. 232 (2) (2011) 142-150.
- [15] A. Barone, F. Fenton, A. Veneziani, Numerical sensitivity analysis of a variational data assimilation procedure for cardiac conductivities, Chaos 27 (2017) 093930. http://dx.doi.org/10.1063/1.5001454.
- [16] J. Stinstra, B. Hopenfeld, R. MacLeod, On the passive cardiac conductivity, Ann. Biomed. Eng. 33 (12) (2005) 1743–1751.
- [17] P. LeGuyader, F. Trelles, P. Savard, Extracellular measurement of anisotropic bidomain myocardial conductivities. i. theoretical analysis, Annals Biomed. Eng. 29 (2001) 862–877.
- [18] R. Sadleir, C. Henriquez, Estimation of cardiac bidomain parameters from extracellular measurement: two dimensional study, Ann. Biomed. Eng. 34 (8) (2006) 1289–1303.
- [19] L.S. Graham, D. Kilpatrick, Estimation of the bidomain conductivity parameters of cardiac tissue from extracellular potential distributions initiated by point stimulation, Ann. Biomed. Eng. 38 (12) (2010) 3630–3648.
- [20] H. Yang, A. Veneziani, Estimation of cardiac conductivities in ventricular tissue by a variational approach, Inverse Problems 31 (11) (2015) 115001.
- [21] I.R. Efimov, et al., Virtual electrode-induced phase singularity: A basic mechanism of defibrillation failure, Circ. Res. 82 (1998) 918–925.
- [22] F.H. Fenton, et al., Termination of atrial fibrillation using pulsed low-energy far-field stimulation, Circulation 120 (2009) 467.
- [23] S. Luther, F.H. Fenton, et al., Low-energy control of electrical turbulence in the heart, Nature 475 (2011) 235-239.
- [24] J. Sundnes, B.F. Nielsen, K.A. Mardal, X. Cai, G.T. Lines, A. Tveito, On the computational complexity of the bidomain and the monodomain models of electrophysiology, Ann. Biomed. Eng. 34 (7) (2006) 1088–1097.
- [25] L. Gerardo-Giorda, L. Mirabella, F. Nobile, M. Perego, A. Veneziani, A model-based block-triangular preconditioner for the bidomain system in electrocardiology, J. Comput. Phys. 228 (10) (2009) 3625–3639.
- [26] L. Gerardo-Giorda, M. Perego, A. Veneziani, Optimized schwarz coupling of bidomain and monodomain models in electrocardiology, ESAIM Math. Model. Numer. Anal. 45 (2) (2011) 309–334.
- [27] L. Mirabella, F. Nobile, A. Veneziani, An a posteriori error estimator for model adaptivity in electrocardiology, Comput. Methods Appl. Mech. Engrg. 200 (37–40) (2011) 2727–2737.
- [28] A. Gizzi, E.M. Cherry, R.F. Gilmour Jr., S. Luther, S. Filippi, F.H. Fenton, Effects of pacing site and stimulation history on alternans dynamics and the development of complex spatiotemporal patterns in cardiac tissue, Front. Physiol. 4 (2013) 1–20.
- [29] H. Yang, A. Veneziani, Efficient estimation of cardiac conductivities via pod-deim model order reduction, Appl. Numer. Math. 115 (2017) 180–199
- [30] J. Keener, J. Sneyd, Mathematical Physiology, Spinger-Verlag, 2009.
- [31] E.M. Cherry, F.H. Fenton, Effects of boundaries and geometry on the spatial distribution of action potential duration in cardiac tissue, J. Theoret. Biol. 285 (2011) 164–176.
- [32] G.A. Holzapfel, R.W. Ogden, Constitutive modelling of passive myocardium: a structurally based framework for material characterization, Phil. Trans. R. Soc. A 367 (2009) 3445–3475.
- [33] C.C. Mitchell, D.G. Schaeffer, A two-current model for the dynamics of cardiac membrane, Bull. Math. Biol. 65 (5) (2003) 767–793.
- [34] F.H. Fenton, A. Karma, Vortex dynamics in three-dimensional continuous myocardium with fiber rotation: Filament instability and fibrillation, Chaos 8 (1998) 20–47.
- [35] A. Bueno-Orovio, E.M. Cherry, F.H. Fenton, Minimal model for human ventricular action potentials in tissue, J. Theoret. Biol. 7 (2008) 544-560.
- [36] F.H. Fenton, E.M. Cherry, Models of cardiac cell, Scholarpedia 3 (2008) 1868.
- [37] D.I. Cairns, F.H. Fenton, E.M. Cherry, Efficient parameterization of cardiac action potential models using a genetic algorithm, Chaos 27 (2017) 093922.
- [38] A. Karma, Electrical alternans and spiral wave breakup in cardiac tissue, Chaos 4 (1994) 461-472.
- [39] F.H. Fenton, E.M. Cherry, H.M. Hastings, S.J. Evans, Multiple mechanisms of spiral wave breakup in a model of cardiac electrical activity, Chaos 12 (3) (2002) 852–892.
- [40] F. Tröltzsch, Optimal Control of Partial Differential Equations: Theory, Methods, and Applications, Vol. 112, American Mathematical Soc., 2010.
- [41] M.D. Gunzburger, Perspectives in Flow Control and Optimization, Vol. 5, SIAM, Philadelphia, PA, 2003.
- [42] L. Bertagna, S. Deparis, L. Formaggia, D. Forti, A. Veneziani, The LifeV library: engineering mathematics beyond the proof of concept, arXiv preprint arXiv:1710.06596.

- [43] M. Heroux, R. Bartlett, V.H.R. Hoekstra, J. Hu, T. Kolda, R. Lehoucq, K. Long, R. Pawlowski, E. Phipps, A. Salinger, H. Thornquist, R. Tuminaro, J. Willenbring, A. Williams, An Overview of Trilinos, Tech. Rep. SAND2003-2927, Sandia National Laboratories, 2003.
- [44] T. Passerini, A. Quaini, U. Villa, A. Veneziani, S. Canic, Validation of an open source framework for the simulation of blood flow in rigid and deformable vessels, International journal for numerical methods in biomedical engineering 29 (11) (2013) 1192–1213.
- [45] I. Uzelac, Y.C. Ji, D. Hornung, J. Schröder-Scheteling, S. Luther, R.A. Gray, E.M. Cherry, F.H. Fenton, Simultaneous quantification of spatially discordant alternans in voltage and intracellular calcium in langendorff-perfused rabbit hearts and inconsistencies with models of cardiac action potentials and ca transients, Front. Physiol. 8 (2017) 819.
- [46] E. Beretta, A. Manzoni, L. Ratti, A reconstruction algorithm based on topological gradient for an inverse problem related to a semilinear elliptic boundary value problem, Inverse Problems 33 (3) (2017) 035010.
- [47] E. Beretta, C. Cavaterra, M.C. Cerutti, A. Manzoni, L. Ratti, An inverse problem for a semilinear parabolic equation arising from cardiac electrophysiology, Inverse Problems 33 (10) (2017) 105008.
- [48] E. Beretta, M.C. Cerutti, A. Manzoni, D. Pierotti, An asymptotic formula for boundary potential perturbations in a semilinear elliptic equation related to cardiac electrophysiology, Math. Models Methods Appl. Sci. 26 (04) (2016) 645–670.
- [49] H. Lim, W. Cun, Y. Wang, R.A. Gray, J. Glimm, The role of conductivity discontinuities in design of cardiac defibrillation, Chaos 28 (2018) 013106.
- [50] S. Pezzuto, J. Hake, J. Sundnes, Space-discretization error analysis and stabilization schemes for conduction velocity in cardiac electrophysiology, Int. J. Numer. Methods Biomed. Eng. 32 (10) (2016) e02762.
- [51] J. Jilberto, D.E. Hurtado, Semi-implicit non-conforming finite-element schemes for cardiac electrophysiology: a framework for mesh-coarsening heart simulations, Front. Physiol. 9 (2018) 1513.
- [52] S. Brandstaeter, A. Gizzi, S.L. Fuchs, A.M. Gebauer, R.C. Aydin, C.J. Cyron, Computational model of gastric motility with activestrain electromechanics, ZAMM 98 (12) (2018) 2177–2197.
- [53] D.E. Hurtado, D. Rojas, Non-conforming finite-element formulation for cardiac electrophysiology: an effective approach to reduce the computation time of heart simulations without compromising accuracy, Comput. Mech. 61 (2018) 485–497.
- [54] F.H. Fenton, A. Gizzi, C. Cherubini, N. Pomella, S. Filippi, Role of temperature on nonlinear cardiac dynamics, Phys. Rev. E 87 (2013) 042709.
- [55] A. Gizzi, A. Loppini, E.M. Cherry, C. Cherubini, F.H. Fenton, S. Filippi, Multi-band decomposition analysis: Application to cardiac alternans as a function of temperature, Physiol. Meas. 38 (2017) 833–847.
- [56] D.D. Chen, R.A. Gray, I. Uzelac, C. Herndon, F.H. Fenton, Mechanism for amplitude alternans in electrocardiograms and the initiation of spatiotemporal chaos, Phys. Rev. Lett. 118 (2017) 168101.
- [57] A. Loppini, A. Gizzi, R. Ruiz-Baier, C. Cherubini, F.H. Fenton, S. Filippi, Competing mechanisms of stress-assisted diffusivity and stretch-activated currents in cardiac electromechanics, Front. Physiol. 9 (2018) 1714.
- [58] P. Le Guyader, F. Trelles, P. Savard, Extracellular measurement of anisotropic bidomain myocardial conductivities. i. theoretical analysis, Ann. Biomed. Eng. 29 (10) (2001) 862–877.
- [59] P.C. Franzone, L. Pavarino, B. Taccardi, Simulating patterns of excitation, repolarization and action potential duration with cardiac bidomain and monodomain models, Math. Biosci. 197 (1) (2005) 35–66.
- [60] P.C. Franzone, L.F. Pavarino, S. Scacchi, Mathematical Cardiac Electrophysiology, Vol. 13, Springer, 2014.
- [61] F.S. Costabal, F.A. Concha, D.E. Hurtado, E. Kuhl, The importance of mechano-electrical feedback and inertia in cardiac electromechanics, Comput. Methods Appl. Mech. Engrg. 320 (2017) 352–368.
- [62] D.E. Hurtado, S. Castro, A. Gizzi, Computational modeling of non-linear diffusion in cardiac electrophysiology: A novel porous-medium approach, Comput. Methods Appl. Mech. Engrg. 300 (2016) 70–83.
- [63] S. Niederer, L. Mitchell, N. Smith, G. Plank, Simulating human cardiac electrophysiology on clinical time-scales, Front. Physiol. 2 (2011) 14.
- [64] E. Vigmond, F. Vadakkumpadan, V. Gurev, H. Arevalo, M. Deo, G. Plank, N. Trayanova, Towards predictive modelling of the electrophysiology of the heart, Exp. Physiol. 94 (5) (2009) 563–577.
- [65] C.M. Costa, G. Plank, C.A. Rinaldi, S.A. Niederer, M.J. Bishop, Modeling the electrophysiological properties of the infarct border zone, Front. Physiol. 9 (356) (2018).
- [66] F.O. Campos, Y. Shiferaw, R.W. dos Santos, G. Plank, M.J. Bishop, Microscopic isthmuses and fibrosis within the border zone of infarcted hearts promote calcium-mediated ectopy and conduction block, Front. Phys. 6 (57) (2018).
- [67] A. Loppini, A. Gizzi, C. Cherubini, E.M. Cherry, F.H. Fenton, S. Filippi, Spatiotemporal correlation uncovers characteristic lengths in cardiac tissue, Phys. Rev. E 100 (2) (2019) 020201.
- [68] J. Némec, J. Kim, G. Salama, Optical Mapping: Its Impact on Understanding Arrhythmia Mechanisms, John Wiley & Sons, Ltd, 2012, pp. 69–78, Ch. 8.
- [69] M. Tanha, S.K. Chakraborty, B. Gabris, A. Waggoner, G. Salama, D. Yaron, Computational and experimental characterization of a fluorescent dye for detection of potassium ion concentration, J. Phys. Chem. A 118 (2014) 9837–9843.
- [70] T. Krogh-Madsen, A.F. Jacobson, F.A. Ortega, D.J. Christini, Global optimization of ventricular myocyte model to multi-variable objective improves predictions of drug-induced torsades de pointes, Front. Physiol. 8 (1059) (2017).
- [71] S. Filippi, A. Gizzi, C. Cherubini, S. Luther, F.H. Fenton, Mechanistic insights into hypothermic ventricular fibrillation: the role of temperature and tissue size, Europace 16 (2014) 424–434.
- [72] A. Gizzi, A. Loppini, R. Ruiz-Baier, A. Ippolito, A. Camassa, A. La Camera, E. Emmi, L. Di Perna, V. Garofalo, C. Cherubini, S. Filippi, Nonlinear diffusion & thermo-electric coupling in a two-variable model of cardiac action potential, Chaos 27 (2017) 093919.
- [73] C. Cherubini, S. Filippi, A. Gizzi, R. Ruiz-Baier, A note on stress-driven anisotropic diffusion and its role in active deformable media, J. Theoret. Biol. 430 (2017) 221–228.